

# Impact of Temperature Ratio on Overall Cooling Performance: Low-Order-Model-Based Analysis of Experiment Design

**Aravin Dass Naidu**

Department of Engineering Science,  
University of Oxford,  
Parks Road,  
Oxford OX1 3PJ, UK  
e-mail: aravin.naidu@st-annes.ox.ac.uk

**Thomas Povey<sup>1</sup>**

Department of Engineering Science,  
University of Oxford,  
Parks Road,  
Oxford OX1 3PJ, UK  
e-mail: thomas.povey@eng.ox.ac.uk

*This paper describes low-order-model-based analysis of the design of an experiment to be used for parametric studies of adiabatic film and overall cooling effectiveness for fully cooled systems (internal and film) under wide ranges of mainstream-to-coolant temperature ratio variation, in the range  $0.50 < T_{om}/T_{oc} < 2.30$ . The purpose is to improve understanding of—and validation of—the scaling process from typical rig conditions to engine conditions. We are primarily interested in the variation in overall effectiveness when the controlling non-dimensional groups change in a natural co-dependent way with changes in temperature ratio: that is, the practical situation of interest to engine designers. We distinguish this from the situation in which individual non-dimensional groups are varied in isolation: a situation that we believe is essentially impossible to meaningfully approximate in practice, despite a body of literature purporting to do the same. Design and commissioning data from a new high temperature (600 K) test facility is presented, with detailed uncertainty analysis. We show (using a low-order model) that a typical nozzle guide vane which at engine conditions ( $TR = 2.00$ ) would have overall cooling effectiveness of 0.450, would be expected to have overall effectiveness of 0.418 at typical rig conditions ( $TR = 1.20$ ). That is, typical scaling from engine-to-rig result is  $-7.1\%$  and typical scaling from rig-to-engine is  $+7.7\%$ . This result is important for first order estimation of overall cooling performance at engine conditions. [DOI: 10.1115/1.4062279]*

**Keywords:** fluid dynamics and heat transfer phenomena in compressor and turbine components of gas turbine engines, heat transfer and film cooling, measurement techniques, turbine blade and measurement advancements

## Introduction

There are a number of papers in the open literature that discuss the scaling of overall cooling effectiveness ( $\theta$ ) and adiabatic film effectiveness ( $\eta$ ) results. Some of these results have been used as the basis for scaling between typical rig and engine conditions, a matter that is of particular interest to designers. There is, a validation gap, however, in that there are limited laboratory experiments which operate across the full range of engine realistic temperature ratios (TRs). The purpose of the facility described in this paper is to bridge this gap, providing robust data over a wide range of temperature ratios from  $0.50 < T_{om}/T_{oc} < 2.30$  to help understand, and directly validate the scaling process between rig and engine conditions.

In this paper, the high temperature test facility design and operation are described, including the cooling system design and evaluation. We include key experimental commissioning data, computational fluid dynamics (CFD) based predictions of adiabatic film effectiveness trends with temperature ratio, and conjugate predictions (low-order model) of overall cooling effectiveness.

To put the facility in context, we now briefly review the literature. We do this under four headings: high temperature test facilities; adiabatic film effectiveness studies; overall cooling effectiveness studies; and scaling methods.

**High Temperature Test Facilities.** In this section we review existing high temperature (above 500 K) non-rotating test facilities

used for turbine cooling studies. We organize the literature into three sections: flat-plate facilities; annular cascade facilities; and annular engine component facilities.

**Flat-Plate Facilities.** Baldauf et al. [1,2] obtained adiabatic film effectiveness and heat transfer coefficient ( $h$ ) distributions on cooled flat-plates in a flat-plate test facility operating at up to 550 K. The facility was heated with electric air heaters. Straub et al. [3] used a flat-plate test facility to measure overall cooling effectiveness and for heat flux measurements. The facility could operate at up to 1300 K, and was downstream of a combustor.

**Annular Cascade Facilities.** Wiers et al. [4] describe both cold (up to 303 K) and hot (up to 1025 K) annular cascade facilities for aerothermal tests of nozzle guide vanes. In the hot facility, the vanes were positioned downstream of a combustor and the facility used to study the thermal performance of film cooled parts.

**Annular Engine Component Facilities.** Paniagua et al. [5] describe the design and development of a turbine test facility with both a linear cascade and fully-annular engine component test section. The linear and annular test sections were developed to allow optical measurement techniques to be used for flow visualization for proof-of-concept studies and validation studies respectively. Both facilities are supplied either by heated air from natural gas fired heaters (up to 1000 K) or by electric air heaters (up to 900 K). This air is mixed with relatively cool air resulting in mainstream temperatures up to 700 K prior to entering the working section.

Messenger and Povey [6] describe the design of a blowdown-type fully-annular nozzle guide vane test facility (ECAT+), in which heated air (up to 600 K) is stored in pressurized tanks. This

<sup>1</sup>Corresponding author.

Contributed by the Heat Transfer Division of ASME for publication in the JOURNAL OF TURBOMACHINERY. Manuscript received July 18, 2022; final manuscript received March 21, 2023; published online June 9, 2023. Assoc. Editor: Stephen Lynch.

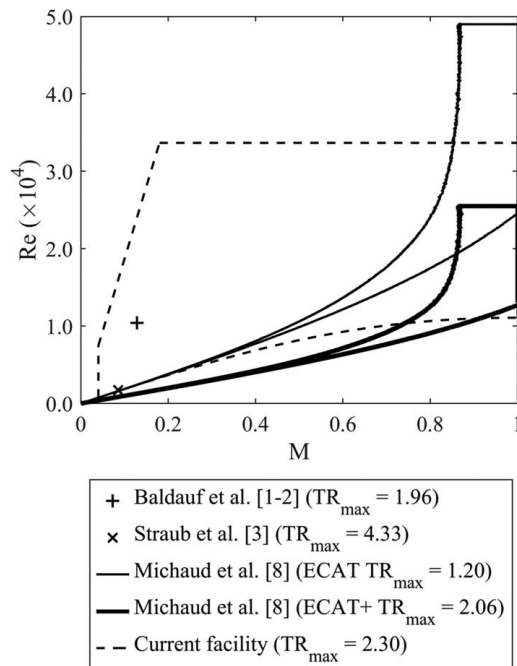


Fig. 1 Survey of facility operating conditions

facility is an upgrade of the Engine Component Aerothermal Facility (ECAT) described in Kirollos et al. [7]. The facilities are used to study the aerothermal performance of nozzle guide vanes. Michaud et al. [8] describe the operational range of both ECAT and ECAT+.

In Fig. 1 we plot the operational range of Reynolds number based on hole-diameter ( $Re_D$ ) and Mach number ( $M$ ) for the flat-plate test facility described in this paper. Existing facilities for which information is provided are also compared. The current facility is unique in that it has been designed to operate over an extremely wide range of Reynolds number, Mach number, and temperature ratio. This gives unique capability for fundamental studies of scaling issues.

**Adiabatic Film Cooling Effectiveness Studies.** In this section we review adiabatic film effectiveness studies under three categories: tests using foreign gas for coolant; tests using cooled cooling air for coolant; and tests using heated mainstream air.

**Tests Using Foreign Gas as Coolant.** In typical large civil jet-engines, the mainstream-to-coolant temperature ratio is approximately  $TR = 2.00$ . This temperature ratio can be achieved in laboratories either by heating the mainstream air or by cooling the coolant air. Both techniques can lead to complexity and cost in facility operation. In an attempt to avoid this, techniques involving so-called foreign gas mixtures have been used (see Jones [9]). No combination of foreign gases exists, however, that is capable of simultaneously matching all relevant non-dimensional groups for aerodynamics and heat transfer conditions relevant to the high- $TR$  condition.

There is a body of work which studies the impact of density ratio ( $DR$ ) on adiabatic film effectiveness, with studies generally conducted in flat-plate test facilities using foreign gases as coolants (see, for example, Perderson et al. [10]; Teekaram et al. [11]; Liu et al. [12]; and Narzary et al. [13]). In some of these studies, engine-like mainstream-to-coolant density ratios were successfully simulated, but in all cases other important non-dimensional groups (specific heat capacity flux, for example) were mis-matched to engine conditions, and the data were not scaled in respect of these mis-matched groups. This—of course—is a fundamental limitation of the foreign-gas technique, and the usefulness of studying the

variation in film effectiveness in respect of a single parameter in isolation might be questioned in a more holistic framework for this problem. This issue is discussed in detail in Ornano and Povey [14].

**Tests Using Cooled Cooling Air.** The majority of film cooling experiments that directly simulate engine-like temperature ratios do so through the use of cooled coolant air. Thole et al. [15] and Sinha et al. [16] measured adiabatic film effectiveness of a film cooled flat-plate over a temperature ratio range of 1.20–2.00. A liquid nitrogen heat exchanger was used to cool the coolant air in a closed-loop wind tunnel test facility. Ethridge et al. [17] measured adiabatic film effectiveness on a simulated film cooled turbine blade at temperature ratios of 1.20 and 1.60. Their experiments were carried out in a closed-loop linear cascade that used coolant air cooled by means of a liquid nitrogen heat exchanger.

**Tests Using Heated Mainstream Air.** Baldauf et al. [18,19] present correlations for adiabatic film effectiveness and heat transfer coefficient from tests carried out on a film cooled flat-plate. Data were obtained over a temperature ratio range of 1.20–1.80 in an open-loop wind tunnel test facility by electrically heating the mainstream air.

**Overall Cooling Effectiveness Studies.** In this section we review overall cooling effectiveness studies.

Dees et al. [20,21] present both experimental measurements and computational predictions of overall cooling effectiveness for an internally (no film cooling) cooled turbine blade. The experiments were carried out in a closed-loop linear cascade that uses cooled coolant air (liquid nitrogen heat exchanger) operated at a temperature ratio of approximately 1.20. The data were used to validate CFD predictions and to demonstrate the effect of rib turbulators on internal cooling. The same cascade was used in the studies of Dees et al. [22], Dyson et al. [23], and Nathan et al. [24]. In these studies, overall cooling effectiveness measurements of a turbine blade with both internal and film cooling were taken and the results were used to both validate CFD predictions and quantify the cooling improvement with film cooling. In their experiments, the Biot number (based on external heat transfer coefficient) and ratio of external and internal heat transfer coefficients were matched to the engine condition. The argument is made that this sufficient for the overall cooling effectiveness to be non-dimensionally matched to the engine condition. This is approximately true: we discuss secondary effects in the next section.

Luque et al. [25] and Luque and Povey [26] describe an open-loop annular sector facility used for engine parts testing. The facility uses a heater mesh to heat mainstream air up to a mainstream-to-coolant temperature ratio of 1.20. Overall cooling effectiveness measurements are taken on a range of nozzle guide vanes from modern civil engines. The facility was used to compare cooling performance for different cooling schemes. In later work, Luque et al. [27] showed that dendritic cooling structures improved overall cooling effectiveness of an NGV even with reduced coolant mass flow. The facility was also used to assess differences between cast and sintered (metal printed) parts in overall cooling effectiveness testing: Kirollos and Povey [28] demonstrated the utility of metal sintered parts for rapid (in-design-loop) assessment of engine components.

To date, most overall cooling effectiveness experiments have been carried out at lower-than-engine mainstream-to-coolant temperature ratios. In some work it has been explicitly argued that engine-scaling is achieved, if external Biot number and the ratio of external-to-internal heat transfer coefficients are matched. In other work this appears to be an implicit assumption. A prime purpose of the present facility is to allow studies of the impact of temperature ratio: that is, the effect of independently varying this group, whilst keeping other non-dimensional groups matched. This will test assumptions made in previous literature and will validate correction methodologies if required.

**Scaling Methods.** In this section we discuss the literature related to the scaling of adiabatic film effectiveness and overall cooling effectiveness data between laboratory and engine conditions. It is organized into adiabatic film effectiveness scaling methods and overall cooling effectiveness scaling methods.

**Adiabatic Film Effectiveness Scaling Methods.** Forth et al. [29] and Forth and Jones [30] studied the scaling of adiabatic film effectiveness for a flat-plate and found that for attached films, adiabatic film effectiveness was a strong function of momentum flux ratio. Thole et al. [15] and Sinha et al. [16] also show that momentum flux ratio controls the film jet aerodynamics.

Rutledge and Polanka [31] computationally studied the effect of different scaling parameters on adiabatic film effectiveness and external heat transfer coefficient for a single hole on a turbine blade leading edge. They showed that momentum flux ratio controls the film trajectory and specific heat capacity flux ratio (ER) affects the magnitude of adiabatic film effectiveness.

Ornato and Povey [14] recently developed a more comprehensive theory for the scaling of adiabatic film effectiveness. In this theoretical and computational work, they demonstrate that adiabatic film effectiveness is a function of 11 (additional) non-dimensional groups and argue that—of these—momentum flux ratio, specific heat capacity flux ratio, blowing ratio, and temperature ratio are the four of primary importance. The authors also introduce the concept of region-dependence of the four primary non-dimensional groups, showing that specific groups are dominant in particular regions of the flow. The authors show through CFD studies that in the region close to the hole adiabatic film effectiveness is primarily a function of momentum flux ratio and in the region far downstream of the hole adiabatic film effectiveness scales with specific heat capacity flux ratio. The mechanism is that momentum flux ratio is responsible for the aerodynamic development of the film jet (jet trajectory and shape) near the hole, but that far downstream where the flow is partially mixed the relative heat storage capacity of coolant and mainstream are more important. There is sensitivity of film effectiveness to blowing ratio in an intermediate region because it is this parameter that controls the rate of shear between the mainstream flow and mixing film cooling layer, thus controlling the rate of jet destabilization and consequentially coolant and mainstream mixing. Temperature ratio has a direct effect on adiabatic film effectiveness (independent of other non-dimensional groups) through its impact on kinematic viscosity. The Ornato and Povey [14] paper is unique—and possibly important—in the sense that the study was structured to *independently isolate* the effect of these groups. The purpose was to separate the physical mechanisms responsible for changes in adiabatic film effectiveness when the magnitude of *individual* non-dimensional group is varied. Such a study is only possible by artificial control (in CFD; low-order model; or *thought experiment*) of the underlying variables and therefore values of resulting non-dimensional groups. In any practical situation we are aware of (engine operation; low-temperature experiment) variation of any one group would lead to attendant variation in one or more other groups. That is, in any practical situation, it is only the *overall* change in film effectiveness (or overall effectiveness) associated with the simultaneous change in a number of non-dimensional groups that can be measured and studied. Many—and probably the majority—of studies in the open literature fail to fully appreciate this, and purport to isolate changes in effectiveness (film or overall) with variation in a particular parameter (momentum flux ratio, density ratio, etc.) in experiments where the results are conflated with uncontrolled—and often unrecognized—variation in another parameter. This renders the results of limited value. This situation is surprising in field that many believe to be mature.

Our current study could be viewed as almost the polar opposite of the Ornato and Povey [14] study. Rather than trying to isolate the independent contribution of individual non-dimensional groups varied in isolation, here we are primarily interested in the variation in overall effectiveness *when the controlling non-dimensional groups change in a natural co-dependent way with*

*changes in temperature ratio*. That is, we are explicitly interested in the practical situation of co-dependent variation of all non-dimensional groups as temperature ratio is varied between typical rig (TR = 1.2) and engine (TR = 2.0) conditions. We do, in a later section of this paper, attempt a loose decoupling technique to attribute changes in overall effectiveness to variation in various local quantities (film effectiveness; ratio of internal and external heat transfer coefficients; external Biot number; coolant warming factor) but re-emphasize that this is in the practical situation of co-dependent variation of all non-dimensional groups as temperature ratio is varied, and not a study of the effect of variation of temperature ratio in isolation. The only work we are aware of that deals seriously with this latter issue is that of Ornato and Povey [14].

**Overall Cooling Effectiveness Scaling Methods.** Several authors of overall cooling effectiveness studies (see, for example, Dees et al. [20–22], Dyson et al. [23], Nathan et al. [24]) argue that matching external Biot number and ratio of external and internal heat transfer coefficients to the engine condition achieves the same overall cooling effectiveness result in a scaled (lower-than-engine temperature ratios) experiment.

Luque et al. [32] performed a dimensional analysis of the overall cooling effectiveness problem and demonstrate that overall cooling effectiveness is a function of 12 non-dimensional groups. Of these, although external Biot number and the ratio of external-to-internal heat transfer coefficients are clearly particularly important (can be established through sensitivity analysis), the sensitivity to secondary non-dimensional groups (temperature ratio, for example) has not been sufficiently quantified the literature. In a later paper, Luque et al. [33] show that in two experiments with the same momentum flux ratio but different specific heat capacity flux ratios (using air and foreign gas as coolant), the distribution of overall cooling effectiveness on a nozzle guide vane was very similar, but with an offset in the mean value. The authors attribute the similar overall cooling effectiveness distributions to similar aerodynamic behavior within the developing film cooling layer, resulting from matched momentum flux ratio. The offset in mean value was attributed to a change in the ratio of heat capacity of the coolant flow and entrained mainstream gas (change in specific heat capacity flux ratio).

Luque et al. [32] performed a combined theoretical and numerical study into the scaling of overall cooling effectiveness in conjugate heat transfer problems in compressible environments. The objective was to allow comparison of metal temperatures between different temperature boundary conditions (temperature ratios) while appropriately dealing with compressibility effects. A new invariant temperature parameter was proposed, the form of which was related to conventional overall cooling effectiveness definitions, but with the addition of a *recovery and redistribution parameter*. This accounts for the effects of compressibility *throughout* the system, including in regions which are traditionally thought of as incompressible (internal cooling channels) but which are—in fact—subject to the effects of compressibility due to coupling through the wall (conduction). This concept was both new and important, and the proposed recovery and redistribution parameter was proven to be *precisely invariant* in situations with constant fluid properties (dynamic viscosity, specific heat capacity, thermal conductivity, and isentropic exponent). In real systems operating at the same momentum flux ratio (generally matched between experiments) but different temperature ratios, there is generally an associated change in fluid properties between systems. Here, although the effects discussed by Luque et al. [32] are equally applicable, they are conflated with the complex effects described by Ornato and Povey [14] associated with changes due to mis-matched (between systems) specific heat capacity flux ratio and blowing ratio, and changes in volume dilation and kinematic viscosity, caused by temperature ratio changes.

Williams et al. [34] studied the contribution of internal cooling and film cooling to turbine blade overall cooling effectiveness in



experiments using both adiabatic and diabatic blades. They demonstrated that at low momentum flux ratios, cooling films remained attached and overall cooling effectiveness scaled with film effectiveness. An increase in momentum flux ratio resulted in a greater extent of film lift-off and there was a regime in which both adiabatic film effectiveness and overall cooling effectiveness decreased with increasing momentum flux ratio. In their particular experiment, the increase in momentum flux ratio was accompanied by an increase in coolant mass flowrate (and coolant specific heat capacity flux), which resulted in greater heat pick-up in the internal channels (greater internal cooling effect). It is likely that this also led to an increase in film effectiveness due to the increase in coolant-to-mainstream specific heat capacity flux ratio (see Ormano and Povey [14]) until a regime-change associated with film lift-off. At very high momentum flux ratios, the overall cooling effectiveness increased with increasing momentum flux ratio, likely as a result of the increase in coolant-to-mainstream specific heat capacity flux ratio in an already-detached film cooling regime.

## Facility Overview

We now describe the new high temperature test facility designed to study overall cooling performance (adiabatic film and overall cooling effectiveness) over a wide range of temperature ratios. The facility is designed as a transient open-loop blowdown tunnel, with mainstream and coolant drawn from tanks containing dry air. The flow is controlled using an inline pressure regulator and choked venturi nozzles and exhausts directly to the atmosphere. An unusual feature of the facility is the extended operational range of both temperatures and temperature ratios (approximately  $0.50 < T_{0m}/T_{0c} < 2.30$ ) with mainstream flow temperatures in the range  $290 \text{ K} < T_{0m} < 600 \text{ K}$  and coolant flow temperatures in the range  $260 \text{ K} < T_{0c} < 600 \text{ K}$ . To achieve this the facility has two possible feed systems as follows:

- (i) Single 27.6 bar tank feeding both mainstream and coolant; mainstream heated using an in-line electrical air heater to temperatures up to 600 K; optional in-line vortex tube to cool coolant or electric heater to heat coolant.
- (ii) Separate 50 bar tanks to feed mainstream and coolant; mainstream tank pre-heated to temperatures up to 600 K; optional in-line vortex tube to cool coolant or electric heater to heat coolant.

A photograph and schematic layout of the test facility working section are shown in Figs. 2 and 3(a) respectively.



Fig. 2 Photograph of the test facility working section

**Working Section.** The working section is of rectangular cross-section, with a cooled flat-plate test-part that can be made from ceramic or metal. An unusual feature of the facility is the ability to acquire full-surface infrared (IR) images of both the upper and lower surface of the test plate.

Flow in the working section is conditioned with a NEL type flow conditioner (designed from BS EN ISO 5167 [35]) to reduce swirl and establish a uniform velocity profile; a contraction (designed from Morel [36,37] and Su [38]) with a velocity ratio of approximately 4.5) to reduce inlet turbulence, and establish a uniform velocity profile; a turbulence grid (designed using Roach [39]) to establish a particular turbulence length scale and intensity; a boundary layer bleed cassette to bleed off wall boundary layer fluid upstream of the flat-plate; a diffuser (designed from Ishikawa and Nakamura [40]) to recover pressure; and an orifice plate (designed from BS EN ISO 5167 [35]) to control facility outlet pressure. The de-featured schematic of the working section in Fig. 3(c), illustrates the position of some of the above-mentioned components. Burst disks are positioned just upstream of the working section in both the mainstream and coolant feed lines to protect the working section from pressures beyond the design pressure of the facility.

**Instrumentation and Data Acquisition.** The working section is instrumented with inlet total pressure and temperature rakes (six total pressure and six total temperature probes) upstream of the flat-plate, and static pressure tapings both along the working section (12 tapings along the length of the flat-plate), and downstream of the flat-plate. Additional total pressure and temperature probes are located in the coolant plenum to monitor coolant feed conditions. To monitor the overall working section operating condition, total pressure probes and static pressure tapings are also used in the inlet contraction and exit diffuser. Mainstream and coolant mass flowrates are measured using sonic-venturi nozzles (see Fig. 3(a)). The instrumentation positions are shown in Fig. 3(b).

Surface temperatures of the flat-plate are measured with two IR cameras (FLIR A655sc) housed in pressure vessels (for overall facility safety) and separated from the flow path by Zinc Selenide windows. The arrangement is shown in Fig. 3(c). Anti-reflective coatings are used to improve overall transmissivity. In situ calibration of the cameras is achieved via the use of the low-conductivity isothermal-patch method, described in Michaud et al. [41].

**Flat-Plate Design.** The working section is designed to house a cooled rectangular flat-plate, 215 mm by 115 mm in size. Plates can be machined or laser sintered, and the intention is to study engine-like cooling configurations.

In the first build of the facility, two flat-plates are to be installed, a diabatic plate laser sintered from a nickel alloy, and an approximately adiabatic plate machined from ceramic (Macor). These will be used to study the overall cooling effectiveness and corresponding adiabatic film effectiveness distributions over a wide range of mainstream-to-coolant temperature ratios. The design used in the pilot project is shown in Fig. 4. The design is heavily internally and film cooled and features repeating cooled *modules* both in the streamwise (three modules) and lateral (six modules) direction. On the internal side, coolant enters individual modules through a rectangular slot, and passes in the reverse flow direction along an internal channel (4.50 mm high) incorporating 45 deg V-shaped broken rib turbulators (0.50 mm high). Each module exhausts through three equally spaced 2.00 mm diameter circular holes angled at 35 deg to the external wall. The external and internal wall thicknesses were 3.00 mm and 2.00 mm respectively. Local parameters (hole size, hole spacing, wall thicknesses, channel height, etc.) are related to typical engine designs by a scale factor of 2. The global design is based on the reverse pass cooling designs of Kirollos and Povey [42–44] in which the coolant potential decrease and adiabatic film effectiveness decrease are opposed, so that approximately constant overall cooling effectiveness is achieved. This type of design is particularly interesting for the

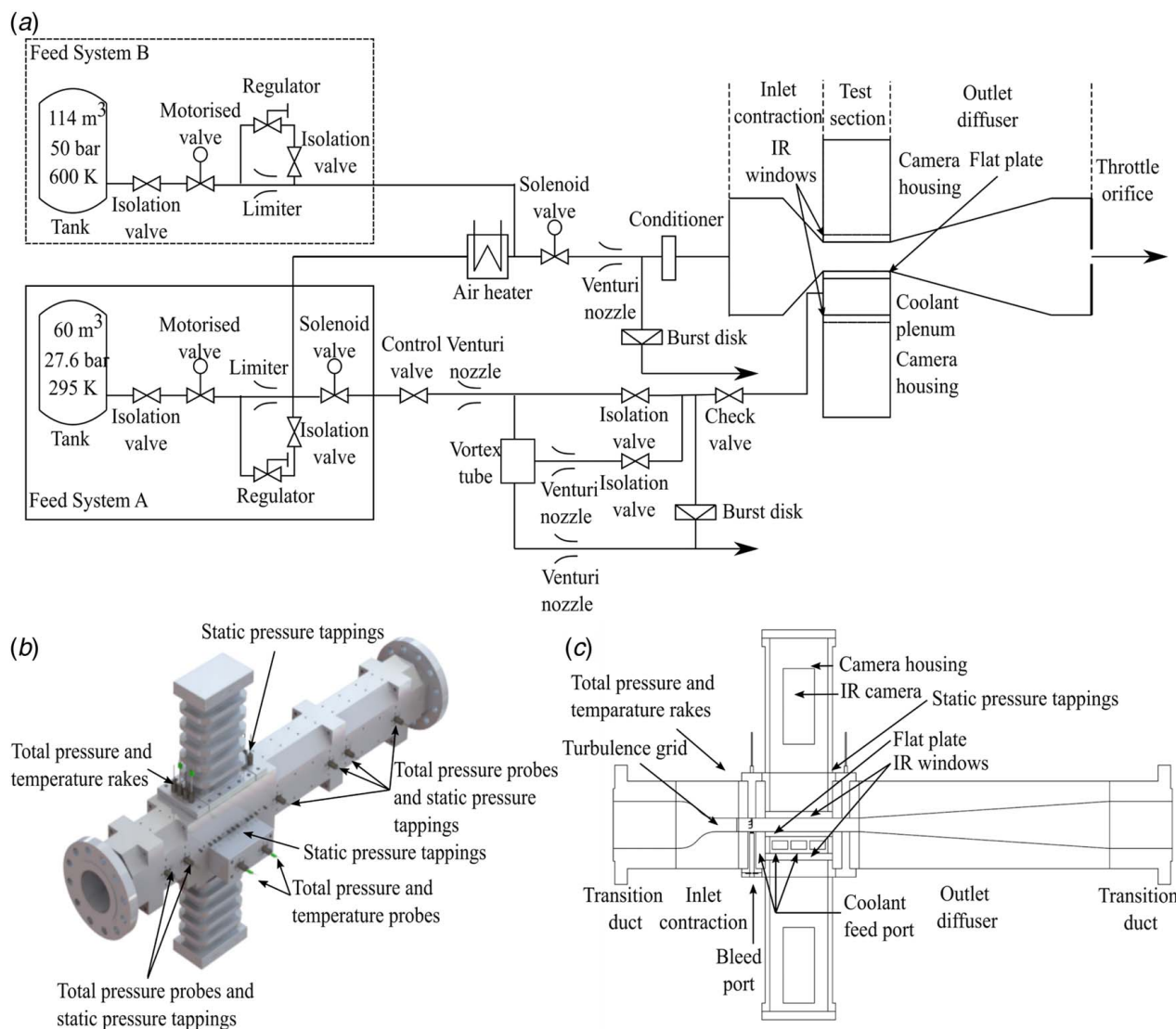


**Fig. 3 Details of the test facility: (a) schematic representation, (b) three-dimensional rendering of the working section, showing instrumentation positions, and (c) defeatured cross-section of the working section, showing infrared cameras and flat-plate test article**

present study because it maximizes the coupling between the internal and external systems. A target external wall overall cooling effectiveness value of  $\theta = 0.50$  was chosen so as to maximize the sensitivity of  $\theta$  to second-order effects arising from dissimilarity of temperature ratio (between facility and engine condition).

### Facility Operating Envelope

Test facility operating conditions are summarized in Table 1. The mainstream total temperature ( $T_{om}$ ) is heated via either an electrical heater (feed system A) or via stored heated air (feed system B) from 290 K to 600 K. Coolant total temperature ( $T_{oc}$ ) is either cooled via a vortex tube to 260 K or heated via an electric heater to 600 K. The resulting coolant-to-mainstream temperature ratio range is  $0.50 < T_{om}/T_{oc} < 2.30$ . This is illustrated in Fig. 5 as a function of  $T_{om}$  and  $T_{oc}$ .

To study the effect of temperature ratio on adiabatic film effectiveness and overall cooling effectiveness, it is necessary to minimize changes in other non-dimensional groups. To maintain constant Reynolds number (here we base it on film hole diameter and mainstream velocity,  $Re_D$ ) for different mainstream temperatures—for example—the inlet total pressure must be adjusted to

account for changing mainstream density (with temperature) and viscosity. The required inlet total mainstream pressure ( $p_{om}$ ) for different inlet total temperatures (for  $Re_D = 1.50 \times 10^4$ ) is shown in Fig. 6. The coolant total pressure ( $p_{oc}$ ) to achieve a coolant-to-mainstream pressure ratio  $p_{oc}/p_{om} = 1.02$  is also shown, as is the static pressure ( $p_m$ ) to achieve a local Mach number ( $M$ ) of 0.30. The range of mainstream temperatures and pressures over which the facility can operate is demarcated by a dashed box. For tests covering the temperature ratio range  $0.50 < T_{om}/T_{oc} < 2.30$ , it is necessary to control the supply total pressure in the range  $1.15 \text{ bar} < p_{om} < 2.80 \text{ bar}$ .

### Facility Commissioning Results

In this section we review commissioning results from runs in which the electrically heated feed system was used (feed system A).

**Pressure and Temperature Characteristics.** Total and static pressures of mainstream and coolant flows are shown Fig. 7(a). Flow is initiated at 10 s, and flow is turned off at 250 s. During the steady period of the run, the pressure is maintained constant to within 0.50% of the target pressure. This is considered relatively

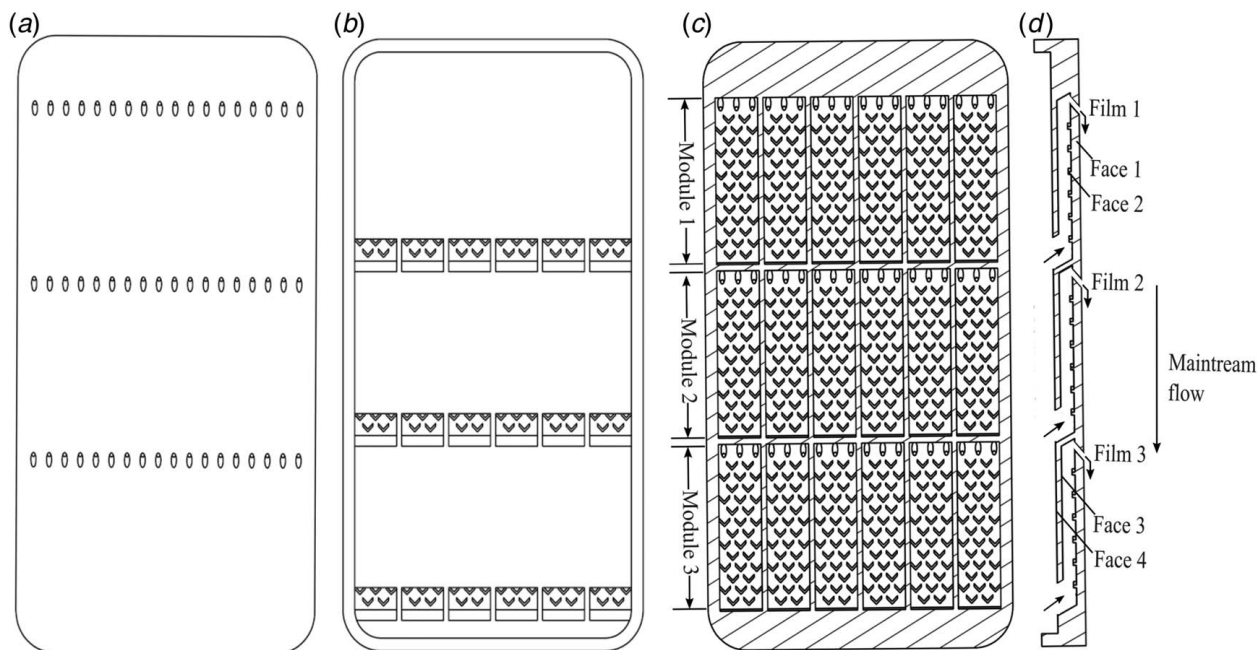


**Fig. 4 Drawings of the flat-plate test article showing: (a) external wall facing the mainstream (face 1), (b) internal wall facing the coolant plenum (face 4), (c) external wall facing the coolant channel showing pedestal bank (face 2), and (d) cross-section**

small for heat transfer testing but could be improved with more precise flow regulation.

The mainstream and coolant total temperature characteristic is shown in Fig. 7(b). The spike in temperature at 30 s is related to isentropic heating during initial pressurization of the facility. The air heater is turned on at approximately 60 s and off at about 230 s. The region in which the facility pressure is within 90% of its maximum value is marked on the figure (the heater is only operated within this period to avoid overheating of the element). Although the heater power is ramped to 100% of its target value within 15 s (60–75 s), the mainstream gas is still increasing in temperature at the end of the run. This is due to the large time constant (approximately 500 s) of the pipe-system between the heater and working section. In contrast, the time constants of the test plate are approximately 12 s on the external wall and 63 s on the internal wall. The time-variation of the measured external and internal wall temperatures are presented in Fig. 7(b) (averaging regions marked in Fig. 8). In practice, quasi-steady conditions of overall cooling effectiveness (defined as a difference in effectiveness of less than 1% between the transient response and the equivalent steady-state value that would be instantaneously achieved) are achieved after approximately 170 s. An extended discussion of these calculations is given in Appendix A.

**Table 1 Test facility operating conditions**

Parameter	Symbol	Range
Mainstream total temperature (K)	$T_{0m}$	290–600
Coolant total temperature (K)	$T_{0c}$	260–600
Coolant-to-mainstream total pressure ratio (–)	$p_{0c}/p_{0m}$	Low to high
Mainstream total pressure (bar)	$p_{0m}$	1–10
Mainstream-to-coolant total temperature ratio (–)	$T_{0m}/T_{0c}$	0.50–2.30
Outlet Reynolds number based on hole diameter (–)	$Re_D$	$1.50 \times 10^4$ – $3.15 \times 10^4$
Outlet Mach number (–)	$M$	0.30–1.00
Turbulence length scale (mm)	$l$	3.00
Turbulence intensity (%)	$Tu$	10.00

**Overall Cooling Effectiveness Measurements.** Full surface overall cooling effectiveness measurements on both the external and internal surfaces of the test plate are shown in Figs. 8(a) and 8(b), respectively. These data are taken for the same run as that shown in Fig. 7 (average between 170 s and 230 s). Here the overall cooling effectiveness,  $\theta$ , is defined by

$$\theta(x, t) = \frac{T_{0m} - T_w(x, t)}{T_{0m} - T_{0c, in}} \quad (1)$$

where we take the common incompressible definition (for discussion see Michaud et al. [45]) because our experiments occur in the Mach number range  $M < 0.30$ .

In Figs. 8(a) and 8(b), the isothermal copper disks used for in situ infrared calibration can be seen as two circular regions of constant overall cooling effectiveness near the top of the images.

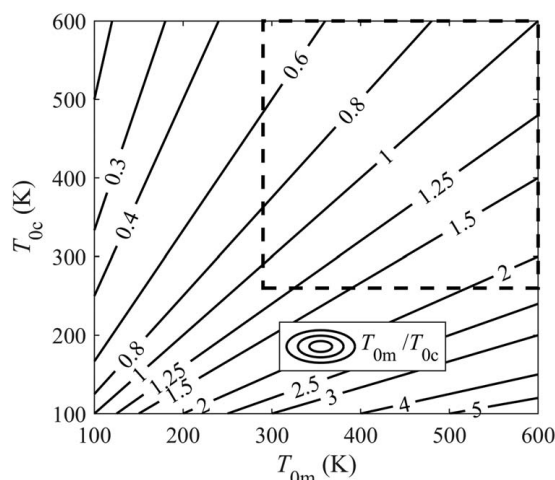


**Fig. 5 Mainstream-to-coolant temperature ratios as a function of absolute mainstream and coolant temperatures. The demarcated dashed box indicates the range over which the facility can operate.**



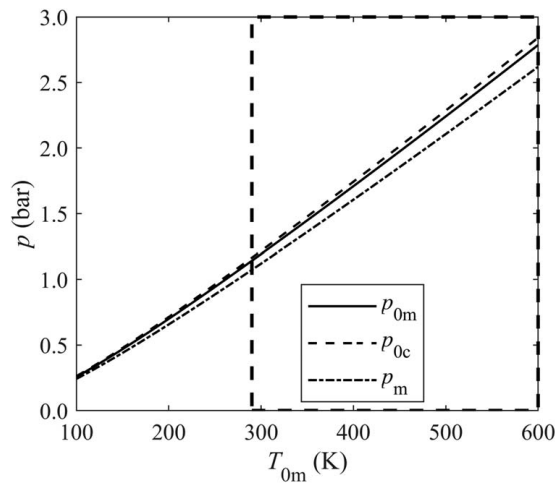


**Fig. 6 Required mainstream and coolant pressures to maintain constant  $Re_D$  over a range of temperature ratios. The demarcated dashed box indicates the range over which the facility can operate.**

On the external surfaces (Fig. 8(a)) the leading edge (LE) and trailing edge (TE) are marked, and the effect of film cooling superposition (increase in film effectiveness in the streamwise direction) is apparent. On the internal wall (Fig. 8(b)) the direction of flow is reversed (reverse pass cooling scheme, as shown in Fig. 4), and

the overall cooling effectiveness decreases in the direction of coolant flow, due to heat pick up in the coolant stream. In both images there is exceptionally good periodicity between the six channels (in the lateral direction) for all three modules (in the streamwise direction), with almost no difference in the lateral direction between modules.

To study the transient behavior of the plate, we consider the transient overall cooling effectiveness characteristics at the external wall locations A1, B1, and C1 and internal wall locations A4, B4, and C4 (marked in Fig. 8). These are presented in Fig. 9. The time-base corresponds to that used in Fig. 7 but only the period between 50 s and 250 s is shown. The initial temperatures of both the metal plate and coolant are close to ambient, and therefore the overall cooling effectiveness is close to unity at the start of the run. Between 170 s and 230 s the overall cooling effectiveness characteristics are stable to within 1% of their average value in this period. We take the result in this period to be steady. On the external wall, during the settled period, the average values of  $\theta$  for regions A1, B1, and C1 are 0.42, 0.48, and 0.52. The data are ordered in terms of increasing effectiveness in the streamwise direction, due to an increase in film effectiveness. The same effect is apparent on the internal wall, with regions A4, B4, and C4 having average values 0.80, 0.84, and 0.86: i.e., an increase in overall cooling effectiveness in streamwise direction of the external surface. Although the three streamwise modules are nominally identical (same flow-rate, same passage design, etc.) the heat pick up within the channel is lower for the trailing channel than the leading channel (nomenclature of external surface) because of improved film performance on the external wall.

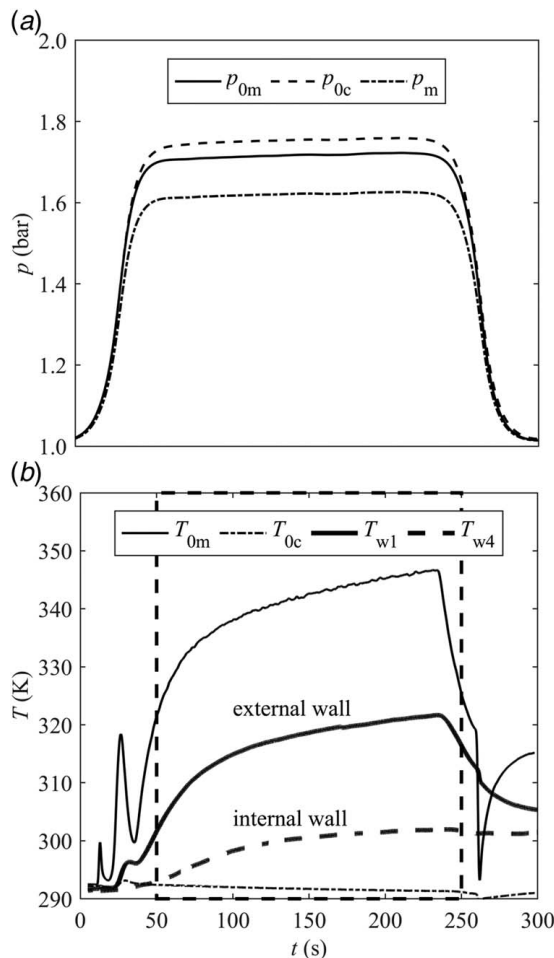


**Fig. 7 Typical facility operating conditions showing: (a) mainstream and coolant pressures and (b) temperatures of mainstream flow, coolant flow, and external and internal wall**

## Effect of Temperature Ratio on Flat-Plate Adiabatic Film Effectiveness and Overall Cooling Effectiveness Distributions

The principal purpose of the facility described in this paper to experimentally determine the variation in adiabatic film effectiveness and overall cooling effectiveness with mainstream-to-coolant temperature ratio for fixed  $Re_D$ ,  $M$ , and  $p_{0c}/p_{0m}$  (the parameters typically matched between laboratory and engine conditions) to help understand of scaling process between temperature ratios. This requires both sufficiently accurate measurement capability, and a flat-plate design with measurable separation between adiabatic film effectiveness and overall cooling effectiveness results at different temperature ratio conditions. To determine whether the facility overall, and the initial flat-plate design in particular, are suitable for this purpose, we perform simulations to determine the predicted adiabatic film and overall cooling effectiveness distributions over the range of temperature ratios  $1.17 < T_{0m}/T_{0c} < 2.00$ . This somewhat arbitrary range covers the typical range between typical laboratory ( $T_{0m}/T_{0c} \sim 1.17$ ) and engine ( $T_{0m}/T_{0c} \sim 2.00$ ) conditions. We refer to the case with  $T_{0m}/T_{0c} = 2.00$  as the reference case for the purpose of comparisons of simulations at different temperature ratios. The work is split into two parts: CFD predictions of adiabatic film effectiveness distributions; and overall cooling effectiveness distribution predictions using a low-order conjugate thermal model.

**Computational Fluid Dynamics Predictions of Adiabatic Film Effectiveness Distribution.** CFD predictions of *adiabatic* film cooling effectiveness are necessary for two purposes: firstly, to demonstrate that there is likely to be a measurable separation between adiabatic film effectiveness distributions over the range of facility temperature ratios for fixed  $Re_D$ ,  $M$ , and  $p_{0c}/p_{0m}$  (i.e., dissimilarities caused by temperature ratio effects at typical laboratory boundary conditions); and secondly as an input to the low-order conjugate model to answer the same question for the overall cooling effectiveness distributions. Here adiabatic film

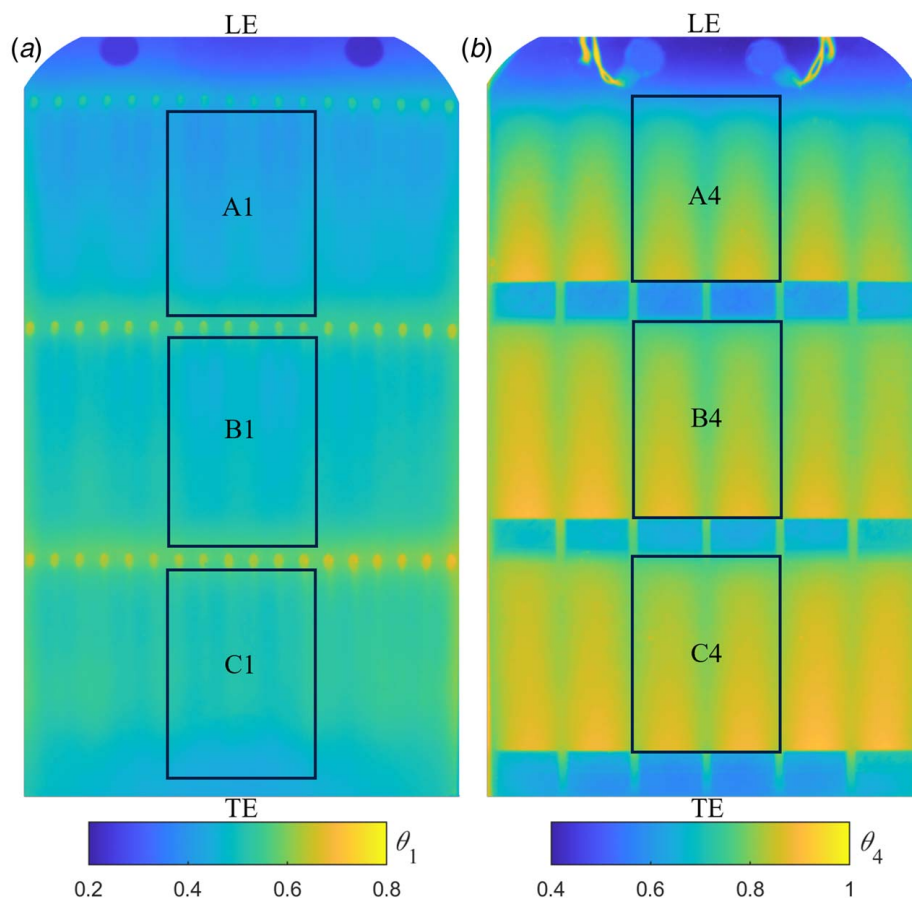


**Fig. 8 Overall cooling effectiveness measurements for the metal test-plate (data for  $t = 200$  s in Fig. 7(b)): (a) external wall and (b) internal wall**

effectiveness is defined by

$$\eta(x) = \frac{T_{0m} - T_{aw}(x)}{T_{0m} - T_{0c,out}} \quad (2)$$

RANS CFD simulations were carried out in ANSYS CFX using the high-resolution advection scheme and  $k-\omega$  SST turbulence model

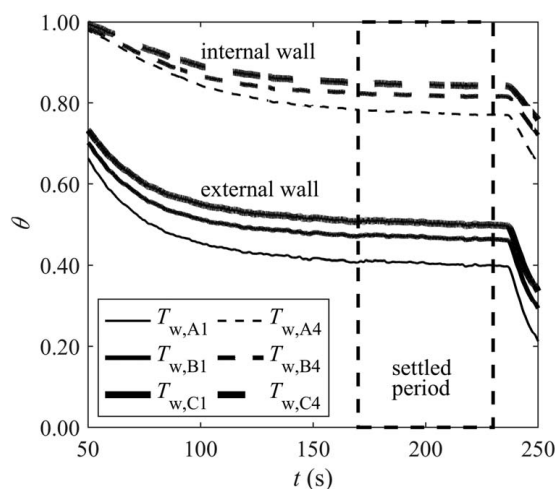


**Fig. 9 Overall cooling effectiveness characteristics for the metal test-plate for three wall locations on each of the external and internal walls. The demarcated box indicates the period in which the solution is within 1% of the instantaneously steady value.**

with automatic wall functions. The numerical domain is shown in Fig. 10.

At the mainstream and coolant domain inlets, the total temperature, total pressure, turbulence intensity, turbulence length scale, and flow direction were prescribed. The domain outlet boundary condition was specified with a constant outlet static pressure. Periodic boundaries were used on the sides of the domain. Fluid properties for air were used, with temperature dependent properties ( $c_p$ ,  $k$ , and  $\mu$ ) from Pofert et al. [46,47]. Cases were run at six temperature ratios ( $T_{0m}/T_{0c} = 1.17, 1.33, 1.50, 1.67, 1.83$ , and  $2.00$ ), with the mainstream total and static pressure chosen to keep the

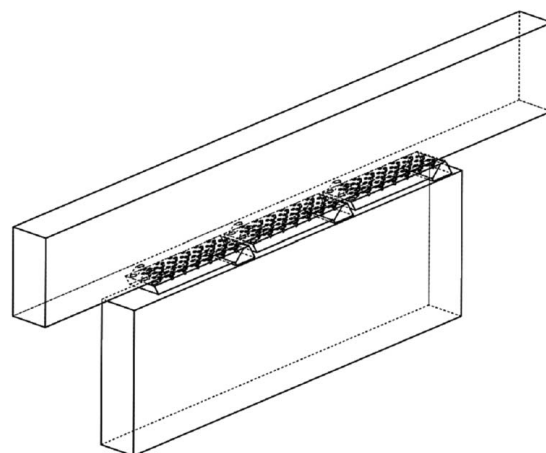


**Fig. 10 The numerical domain**



**Table 2 Summary of CFD boundary conditions and corresponding non-dimensional groups for the different test cases**

Case	$T_{0m}$ (K)	$T_{0c}$ (K)	$p_{0m}$ (bar)	$p_{0c}$ (bar)	$p_{out}$ (bar)	Tu (%)	$L_c$ (mm)	$Re_D$ (–)	M (–)	$T_{0m}/T_{0c}$ (–)	$p_{0c}/p_{0m}$ (–)
1	350	300	1.47	1.49	1.38	10	3	$1.50 \times 10^4$	0.30	1.17	1.02
2	400	300	1.73	1.76	1.62	10	3	$1.50 \times 10^4$	0.30	1.33	1.02
3	450	300	2.00	2.04	1.88	10	3	$1.50 \times 10^4$	0.30	1.50	1.02
4	500	300	2.26	2.31	2.13	10	3	$1.50 \times 10^4$	0.30	1.67	1.02
5	550	300	2.54	2.59	2.39	10	3	$1.50 \times 10^4$	0.30	1.83	1.02
6	600	300	2.81	2.87	2.64	10	3	$1.50 \times 10^4$	0.30	2.00	1.02

mainstream  $Re_D$  and M constant. The coolant total pressure was set to a value to keep  $p_{0c}/p_{0m}$  constant. The conditions are summarized in Table 2.

The mesh is shown in Fig. 11. It was constructed in BOXER-mesh. To demonstrate that the solutions were mesh-independent, a study was conducted using a coarse, medium, and fine mesh (8, 15, and 19 million cells respectively). Here the near wall cell size was halved for each mesh with increasing cell count. Simulations were converged for  $T_{0m}/T_{0c} = 2.00$  (case 6). Distributions of wall shear stress ( $\tau$ ) and adiabatic film effectiveness along the domain centerline of the film cooled wall are shown in Fig. 12. Mesh independence was achieved for the mesh using 15 million cells.

CFD-predicted centerline and laterally-averaged adiabatic film effectiveness distributions are shown in Fig. 13(a) for  $T_{0m}/T_{0c} = 1.17, 1.33, 1.50, 1.67, 1.83$ , and 2.00.

Consider first the case for  $T_{0m}/T_{0c} = 2.00$ . The centerline effectiveness distribution for Module 1 decreases from unity at the hole exit ( $x/L_{cm} = 0$ ) to a minimum value of 0.252 at  $x/L_{cm} = 0.15$ , before increasing again between  $x/L_{cm} = 0.15$  to  $x/L_{cm} = 0.60$  (mean value 0.335 in this range). The minimum at  $x/L_{cm} = 0.15$  is due to jet lift off close to the hole. For Module 2 and Module 3 there is a successive increase in centerline effectiveness due to the film superposition effect. The average centerline effectiveness values for the three modules were 0.380, 0.399, and 0.425, for Modules 1, 2, and 3 respectively.

The laterally-averaged film effectiveness distribution for  $T_{0m}/T_{0c} = 2.00$  (also shown in Fig. 13(a)) shows similar behavior, but with a more pronounced increase (than for centerline effectiveness) in the downstream direction associated with the superposition effect. This is expected due to lateral spreading of the films as they mix out. The average laterally effectiveness values for the three modules were 0.132, 0.192, and 0.265, for Modules 1, 2, and 3 respectively.

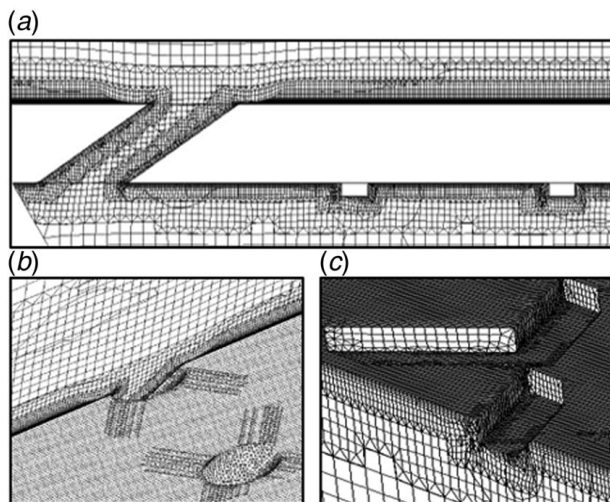


**Fig. 11 Details of mesh showing: (a) near-hole cross-section, (b) near hole surface detail, and (c) detail of ribbed channel section**

Now consider the trend with temperature ratio. With decreasing temperature ratio there is a monotonic decrease in adiabatic film effectiveness both for the centerline values and laterally-averaged values. Differences from the case with  $T_{0m}/T_{0c} = 2.00$  are shown in Fig. 13(b) for the cases  $T_{0m}/T_{0c} = 1.17$  and 1.83. Surface-averaged quantities (between  $0 < x/L_{cm} < 3$ ) are tabulated for all cases in Table 3. The changes in surface-averaged adiabatic film effectiveness (from case with  $T_{0m}/T_{0c} = 2.00$ ) were  $-6.6\%$ ,  $-8.2\%$ ,  $-12.4\%$ ,  $-15.6\%$ , and  $-17.4\%$  for  $T_{0m}/T_{0c} = 1.83, 1.67, 1.50, 1.33$ , and 1.17 respectively. These data are also tabulated in Table 3.

Overall, we see that adiabatic film effectiveness decreases monotonically with decreasing temperature ratio. We now explain this trend using the framework of Ormiano and Povey [14], in which there are four dominant non-dimensional groups: momentum flux ratio, specific heat capacity flux ratio, blowing ratio, and temperature ratio.

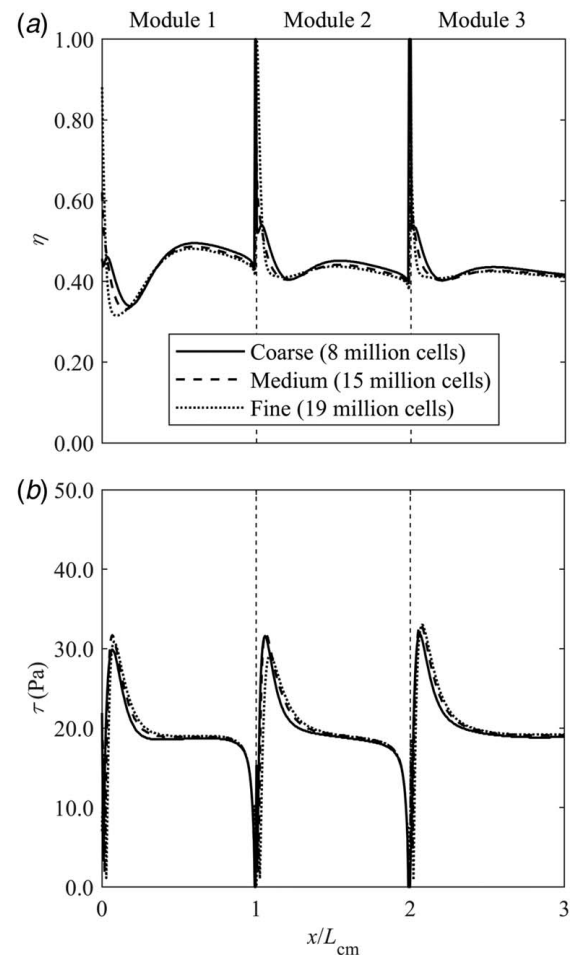


**Fig. 12 Results of mesh sensitivity study for three mesh sizes showing: (a) centerline adiabatic film effectiveness and (b) wall shear stress**

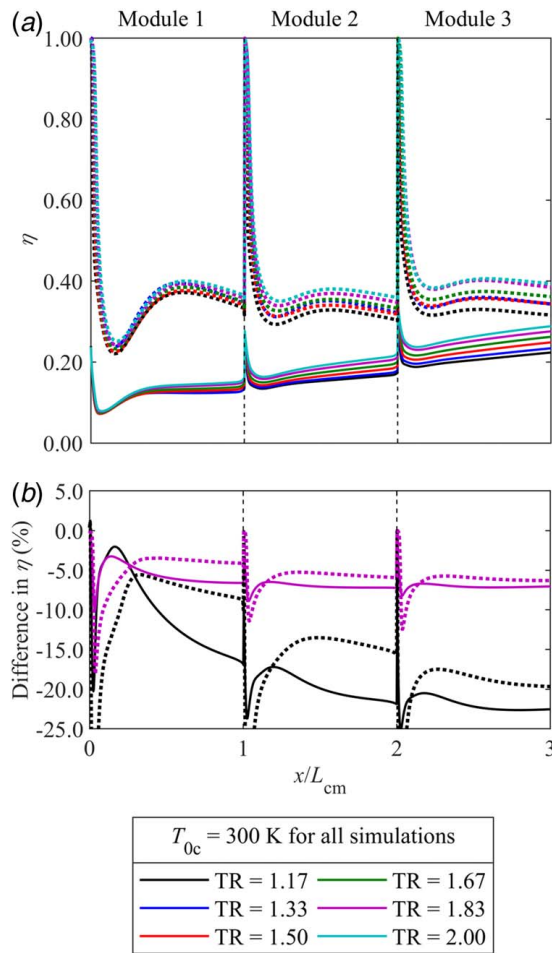


**Fig. 13 (a) Centerline (dotted) and laterally-averaged (solid) adiabatic film effectiveness distributions and (b) differences from the case with  $T_{om}/T_{oc} = 2.00$**

- (i) Because momentum flux ratio is matched between cases with different TR, the primary structure of the flow is unaltered. That is, in our test situation as we change TR there is no effect directly arising from changed momentum flux ratio.
- (ii) With decreasing temperature ratio (and for fixed  $I$ ) there is decrease in the coolant-to-mainstream specific heat capacity flux ratio. Lower relative heat storage capacity in the film results in a greater relative temperature increase due to the mixing of film with the entrained mainstream air. This leads to relatively higher temperature in the mixing layer, and lower film effectiveness. This is the dominant effect in our system.
- (iii) With decreasing temperature ratio (and for fixed  $I$ ) there is a decrease in blowing ratio, and an associated increase in velocity ratio (see Ormano and Povey [14] for mathematical proof). This increase in velocity ratio increases the rate of shear at the film-mainstream interface which leads to greater jet destabilization and greater entrainment-rate of mainstream fluid. This effect is typically almost an order of magnitude smaller than that due to specific heat capacity flux ratio, and is generally confined to a so-called *intermediate region* (an axial region between the region in which the cooling jets have a binary effectiveness distribution, and the mixed our region in which there is full lateral mixing).
- (iv) The direct independent effect of temperature ratio is via the role of kinematic viscosity. In our study TR was decreased by decreasing  $T_{om}$  for fixed  $T_{oc}$ . This results in two effects: firstly, lower kinematic viscosity of the mainstream with

**Table 3 Surface-averaged CFD-predicted adiabatic film effectiveness values ( $\eta_{SA}$ ) at six mainstream-to-coolant TRs, and differences from the case with  $T_{om}/T_{oc} = 2.00$**

$T_{om}/T_{oc}$ (–)	$\eta_{SA}$ (–)	Absolute difference in $\eta$ from case for $T_{om}/T_{oc} = 2.00$ (%)
2.00	0.196	0.0
1.83	0.190	–6.6
1.67	0.180	–8.2
1.50	0.172	–12.4
1.33	0.164	–15.6
1.17	0.159	–17.4

decreasing TR, leading to lower momentum diffusivity, and lower mixing within the near wall region, leading to higher film effectiveness; secondly, there is a reduced volume dilation effect (of coolant layer with entraining mainstream gas) with decreasing TR, leading to—a posited—slightly enhanced entrainment of mainstream gas, leading to slightly lower film effectiveness. These effects are opposed in direction and small in magnitude. Overall the direct impact of temperature ratio (independent of other groups) is believed to be slight.

**Structure of Low-Order Conjugate Thermal Model.** A conjugate thermal model was used to predict the flat-plate overall cooling effectiveness distributions at a range of temperature ratio conditions. The purpose of the model was twofold: to optimize the test article and conditions to achieve measurable separation of results; and to give physical insight into interpretation of experimental results once acquired. A schematic of the model is shown in Fig. 14 (only Modules 1 and 2 are shown). The structure of the model is designed to represent the test article of Fig. 4(d). Advection in the external and internal fluid domain is modeled, as is conduction in the solid and convection at the fluid-solid interface. In the internal cooling channels, the streamwise change in temperature with heat pickup was modeled. The mixing coolant layer was modeled using an entrainment-based approach (mainstream gas entering a mixing layer) with heat loss to the wall. Film superposition calculations were performed using the energy-based method of Kirollos and Povey [48]. In the wall, only through-wall conduction was modeled (no lateral conduction). The overall approach was very similar to that of Kirollos and Povey [42]. The coolant mass flow was calculated with a model based on experimentally-measured plate coolant capacity characteristics (method of Kirollos and Povey [49]), with hole exit static pressures from CFD simulations of the mainstream domain. External Nusselt number distributions were taken from flat plate correlations. Coolant side Nusselt number distributions were taken from Dittus–Boelter-style correlations (turbulent heated flow), with enhancement factors for the ribbed wall. Temperature dependent fluid properties ( $c_p$ ,  $k$ , and  $\mu$ ) of both mainstream and coolant air were calculated using the correlations of Pofert et al. [46,47]. Temperature dependence of thermal properties of nickel alloy is a small effect (see, e.g., Zielinska et al. [50]) and was neglected. We use the terms *face 1*, *face 2*, *face 3*, and *face 4* to refer to the following: the external wall facing the mainstream air; the external wall facing the coolant channel; the internal wall facing the coolant channel; and internal wall facing the coolant plenum. These are shown in (see Fig. 14).

The heat transfer coefficient distributions used for the reference case ( $T_{om}/T_{oc} = 2.00$ ) are shown in Fig. 15(a). The heat transfer coefficient on face 1 ( $h_1$ ) decreases from  $2000 \text{ W m}^{-2} \text{ K}^{-1}$  at the start of Module 1 ( $x/L_{cm} = 0$ ) to  $495 \text{ W m}^{-2} \text{ K}^{-1}$  at the end of Module 3 ( $x/L_{cm} = 3$ ). This decreasing heat transfer coefficient in the streamwise direction is due to the thickening of the boundary layer on the external wall. The area-averaged coolant-side heat transfer coefficients on faces 2 ( $h_2$ ) and 3 ( $h_3$ ) were set to  $410 \text{ W m}^{-2} \text{ K}^{-1}$  and  $135 \text{ W m}^{-2} \text{ K}^{-1}$  respectively. Here  $h_2 > h_3$

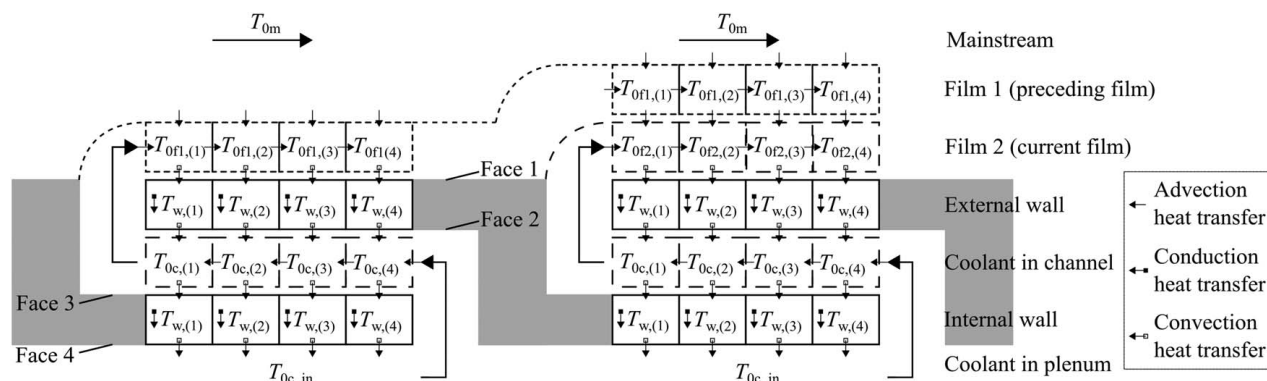


Fig. 14 Schematic representation of the 1.5D steady thermal model (only Modules 1 and 2 are shown)

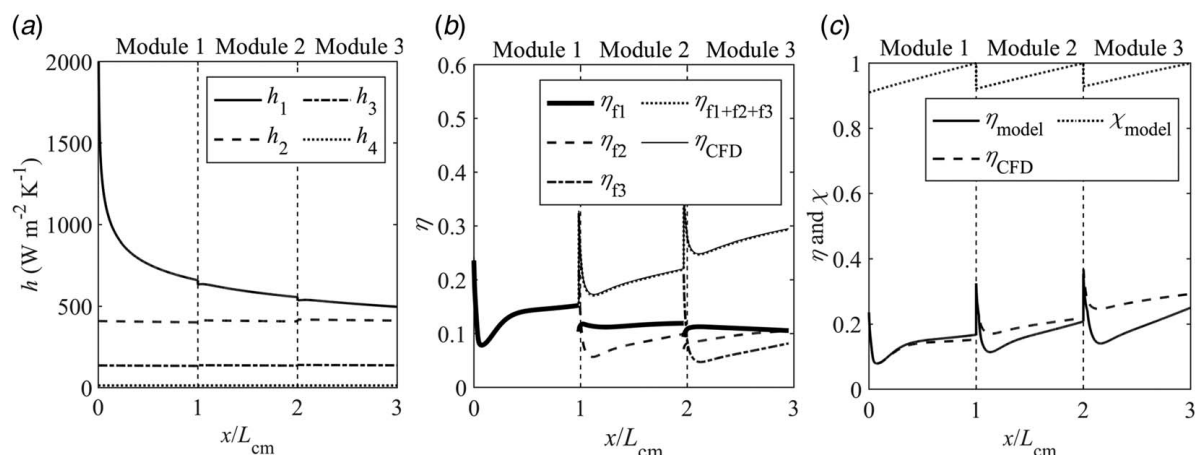


Fig. 15 The case of  $T_{om}/T_{0c} = 2.00$ : (a) heat transfer coefficient distributions for used as inputs to the low-order model, (b) CFD-predicted laterally-averaged adiabatic film effectiveness distributions used as inputs to the low-order model, and (c) film effectiveness distributions and coolant warming factor predicted by the low-order model

to represent enhancement due to rib-turbulators. The area-averaged plenum-side heat transfer coefficient on face 4 was set to  $h_4 = 12 \text{ W m}^{-2} \text{ K}^{-1}$  (very low coolant velocity in plenum).

The adiabatic film effectiveness distributions used in the model are shown in Fig. 15(b). We now describe the procedure for calculating these. The CFD domain of Fig. 10 was solved for reference case conditions ( $T_{om}/T_{0c} = 2.00$ ) using scalar tracking to identify contributions from individual films (method of Thomas and Povey [51]). Walls were set to be adiabatic in the simulations. This allows the *contribution by mass fraction* to laterally-averaged adiabatic film effectiveness associated with each film row to be calculated (see Fig. 15(b)). The superposition (method of Kirollos and Povey [48]) solution of the three films based on mass fractions should be equal to the overall film effectiveness based on the adiabatic wall temperature (also shown in Fig. 15(b)), which confirms the mass fractions evaluated using the scalar tracking method are correct. An equivalent entrained mass flowrate distribution (with axial distance) was then calculated using the method of Kirollos and Povey [48], which—in combination with the particular film flows for the reference case—delivers the predicted adiabatic film effectiveness distribution. This equivalent entrained mainstream mass flowrate distribution is assumed to be the same for all future simulations. To obtain the temperature of each film cell (see Fig. 14) the steady flow energy equation was used, satisfying mass and energy conservation including entrained mainstream gas, and heat lost to the cooled diatomic wall. Because of this latter term, the temperature of the mixing layer (coolant and entrained mainstream gas) is different from the adiabatic film temperature. In analogy with Eq. (2), we define a non-dimensional

temperature for the mixing layer (diabatic system) which we simply refer to as (non-adiabatic) *film effectiveness*. We compare the film effectiveness computed for the diabatic system with the adiabatic film effectiveness obtained from CFD simulations in Fig. 15(c).

We define coolant warming factor,  $\chi(x)$ , as the ratio of the actual heat picked up by coolant in the internal channel to the theoretical maximum heat pick up

$$\chi(x) = \frac{T_{om} - T_{0c}(x)}{T_{om} - T_{0c,in}} \quad (3)$$

Distributions of  $\chi(x)$  are plotted in Fig. 15(c). The coolant warming factor for each module decreases in the direction of the coolant flow (reverse-pass channels) from approximately 1 (inlet) to 0.9 (outlet). For our system the coolant warming factor is everywhere close to unity suggesting that internal cooling effect is primarily limited by the product of heat transfer coefficient and area, rather than by specific heat capacity flux.

**Overall Cooling Effectiveness Distribution Predictions Using Low-Order Conjugate Thermal Model.** In this section we present the results of the low-order conjugate thermal model simulations. The model was run in the temperature ratio range  $1.17 < T_{om}/T_{0c} < 2.00$  for fixed  $Re_D$ ,  $M$ , and  $p_{0c}/p_{0m}$ . Resulting surface overall cooling effectiveness distributions on face 1 ( $\theta_1$ ) are shown in Fig. 16(a). Differences from the nominal TR ( $T_{om}/T_{0c} = 2.00$ ) are presented in Fig. 16(b).



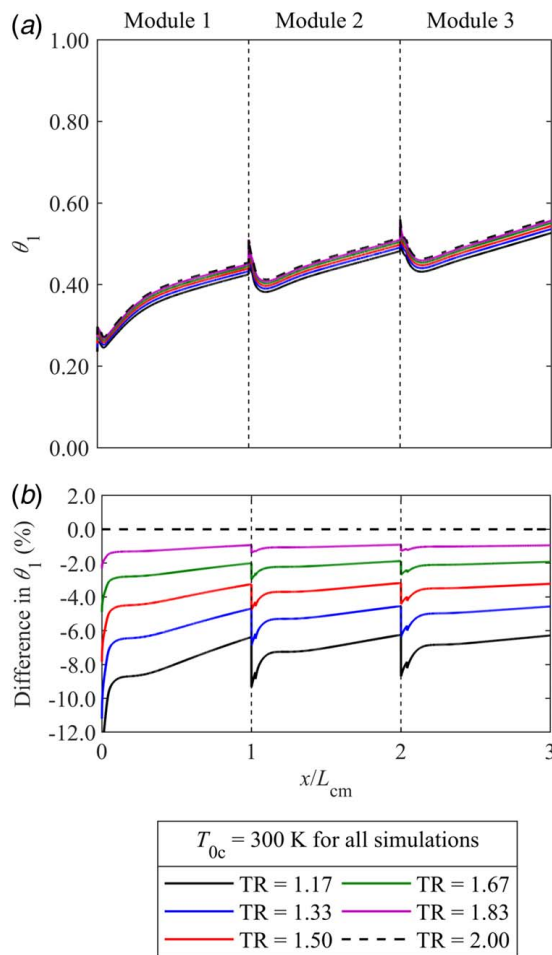


**Fig. 16 Results at six temperature ratios for fixed  $T_{0c} = 300$  K for face 1: (a) overall cooling effectiveness distributions and (b) difference in overall cooling effectiveness from  $T_{0m}/T_{0c} = 2.00$**

We describe the overall cooling effectiveness distribution for the reference case with  $T_{0m}/T_{0c} = 2.00$ . The general trend is that overall cooling effectiveness increases in the direction of the mainstream flow, from a value of approximately 0.30 at the leading edge to a value of approximately 0.55 at the trailing edge. The increase in overall cooling effectiveness in the flow-wise direction is attributed to increasing film effectiveness in the streamwise direction.

Now consider the trend with temperature ratio. The study of this effect is the key purpose of this facility, and therefore this is the result of prime importance. As temperature ratio is decreased, the overall cooling effectiveness on face 1 maintains a similar trend between temperature ratios, but decreases in absolute magnitude. Percentage differences from the reference case are shown in Fig. 16(b). The percentage changes in surface-averaged overall cooling effectiveness on face 1 were  $-1.10\%$ ,  $-2.25\%$ ,  $-3.70\%$ ,  $-5.30\%$ , and  $-7.25\%$  for  $T_{0m}/T_{0c} = 1.83$ ,  $1.67$ ,  $1.50$ ,  $1.33$ , and  $1.17$  respectively. These data are summarized in Fig. 16. The trend is a monotonic decrease in overall cooling effectiveness with decreasing temperature ratio. We attempt a loose explanation of this trend with reference to effects associated with four non-dimensional groups: film effectiveness ( $\eta$ ), the mainstream-to-coolant heat transfer coefficient ratio ( $h_1/h_2$ ), Biot number on face 1 ( $Bi_1$ ), and the cooling warming factor. We do this on the basis of the well-known (see, for example, Nathan et al. [24]) 1D conjugate heat transfer result.

$$\theta_1 = \frac{1 - \chi\eta}{1 + Bi_1 + h_1/h_2} + \chi\eta \quad (4)$$

**Table 4 Low-order model predictions of the values of four important non-dimensional groups for the case of  $TR = 2.00$**

$T_{0m}/T_{0c}$ (—)	Absolute values for reference case				
	$\theta_{1,SA}$ (—)	$\eta_{SA}$ (—)	$\frac{h_{1,SA}}{h_{2,SA}}$ (—)	$\chi_{SA}$ (—)	$Bi_{1,SA}$ (—)
2.00	0.454	0.169	1.568	0.961	0.185

**Table 5 Low-order model predictions of the percentage difference (from case for  $TR = 2.0$ ) in each of four dimensionless groups**

$T_{0m}/T_{0c}$ (—)	Percentage difference case for $TR = 2.00$				
	$\Delta\theta_{1,SA}$ (%)	$\Delta\eta_{SA}$ (%)	$\Delta\frac{h_{1,SA}}{h_{2,SA}}$ (%)	$\Delta\chi_{SA}$ (%)	$\Delta Bi_{1,SA}$ (%)
2.00	0	0	0	0	0
1.83	-1.10	-2.58	1.70	-0.15	-6.36
1.67	-2.25	-5.22	3.60	-0.32	-12.94
1.50	-3.70	-8.70	5.75	-0.51	-19.78
1.33	-5.30	-12.2	8.20	-0.74	-26.84
1.17	-7.25	-16.8	11.0	-1.00	-34.23

**Table 6 Sensitivity coefficients for each of four dimensionless groups for  $TR = 2.0$**

$T_{0m}/T_{0c}$ (—)	Sensitivity coefficients			
	$\frac{\partial\theta_{1,SA}}{\partial\eta_{SA}}$ (—)	$\frac{\partial\theta_{1,SA}}{\partial(h_1/h_2)}$ (—)	$\frac{\partial\theta_{1,SA}}{\partial\chi_{SA}}$ (—)	$\frac{\partial\theta_{1,SA}}{\partial Bi_{1,SA}}$ (—)
2.00	0.612	-0.110	0.108	-0.110

The values of these dimensionless groups for the reference case ( $T_{0m}/T_{0c} = 2.00$ ) and their percentage change from the reference case for simulations with  $T_{0m}/T_{0c} = 2.00$ ,  $1.83$ ,  $1.67$ ,  $1.50$ ,  $1.33$ , and  $1.17$  are summarized in Tables 4 and 5 respectively. Sensitivity coefficients ( $\partial\theta_1/\partial\eta$ ,  $\partial\theta_1/\partial(h_1/h_2)$ ,  $\partial\theta_1/\partial\chi$ , and  $\partial\theta_1/\partial Bi_1$ ) arising from Eq. (4) are summarized in Table 6 (computed for  $T_{0m}/T_{0c} = 2.00$ ). The product of the sensitivity coefficient and the percentage change with  $TR$  in each dimensionless group is summarized in Table 7. Dealing with each of these groups in turn:

- The predicted change (from reference case) in surface-average film effectiveness (from the case with  $T_{0m}/T_{0c} = 2.00$ ) varies between  $-2.58\%$  for  $T_{0m}/T_{0c} = 1.83$  to  $-16.8\%$  for  $T_{0m}/T_{0c} = 1.17$ . Using simple logic, the sensitivity coefficient ( $\partial\theta_1/\partial\eta$ ) between the change in film effectiveness and overall cooling effectiveness might be expected to be approximately unity. From Eq. (4) at the nominal operating point of the plate ( $\theta_1 = 0.454$ ,  $\eta = 0.169$ ,  $h_1/h_2 = 1.568$ ,  $\chi = 0.961$ ,  $Bi_1 = 0.185$ ) a more accurate estimate of the sensitivity coefficient is approximately 0.612. Comparing the changes in film effectiveness and overall effectiveness, taking the sensitivity coefficient into account, we see that this effect accounts for (averaged across all temperature ratios)  $+55.2\%$  of the change in overall effectiveness, and is of first-order importance.
- The predicted change (from reference case) in the ratio of surface-averaged mainstream-to-coolant heat transfer coefficients varies between  $+1.70\%$  for  $T_{0m}/T_{0c} = 1.83$  to  $+11.0\%$  for  $T_{0m}/T_{0c} = 1.17$ . The degree to which this ratio affects the

**Table 7 Product of sensitivity coefficients and the percentage change in each dimensionless group from the case for TR = 2.0**

$\frac{T_{0m}}{T_{0c}}$ (-)	Product of sensitivity coefficient and the percentage change in each dimensionless group from the case for TR = 2.0				Percentage difference from case for TR = 2.0	
	$\frac{\partial \theta_{1,SA}}{\partial \eta_{SA}} \Delta \eta_{SA}$ (%)	$\frac{\partial \theta_{1,SA}}{\partial h_{1,SA}/h_{2,SA}} \Delta \frac{h_{1,SA}}{h_{2,SA}}$ (%)	$\frac{\partial \theta_{1,SA}}{\partial \chi_{SA}} \Delta \chi_{SA}$ (%)	$\frac{\partial \theta_{1,SA}}{\partial Bi_{1,SA}} \Delta Bi_{1,SA}$ (%)	Checksum of individual contributions $\Delta \theta_{1,SA}$ (%)	Model prediction $\Delta \theta_{1,SA}$ (%)
2.00	0	0	0	0	0	0
1.83	-0.69	-0.65	-0.03	0.29	-1.08	-1.10
1.67	-1.29	-1.37	-0.07	0.58	-2.15	-2.25
1.50	-2.08	-2.20	-0.18	0.89	-3.50	-3.70
1.33	-2.88	-3.13	-0.17	1.21	-4.97	-5.30
1.17	-3.93	-4.20	-0.23	1.54	-6.82	-7.25

overall effectiveness is a function of the wall thermal resistance ( $t_w/k_w$ ). At the nominal design point the sensitivity coefficient ( $\partial \theta_1 / \partial (h_1/h_2)$ ) was calculated (using Eq. (4)) to be  $-0.110$ . This effect accounts for  $+60.0\%$  of the change in overall effectiveness, and is of first-order importance.

- (iii) The predicted change (from reference case) in surface-averaged coolant warming factor varies between  $-0.15\%$  for  $T_{0m}/T_{0c} = 1.83$  to  $-1.00\%$  for  $T_{0m}/T_{0c} = 1.17$ . At the nominal operating point of the plate, the sensitivity coefficient ( $\partial \theta_1 / \partial \chi$ ) is approximately  $0.108$ . This effect accounts for  $+4.5\%$  of the change in overall effectiveness. This effect is of second-order importance.
- (iv) The predicted change (from reference case) in surface-averaged Biot number varies between  $-6.36\%$  for  $T_{0m}/T_{0c} = 1.83$  to  $-34.2\%$  for  $T_{0m}/T_{0c} = 1.17$ . Here the sensitivity coefficient ( $\partial \theta_1 / \partial Bi_1$ ) is approximately  $-0.110$ . The Biot number effect accounts for  $-20.0\%$  of the change in overall effectiveness. This effect is of intermediate importance.

As a validation of the simple decomposition approach to determine relative contributions from the four terms, we perform a *checksum* of the individual contributions (simple addition of uncoupled terms) and compare this to the direct output of the model (result from fully coupled boundary conditions). These are compared in Table 7. Differences agree to within 6% of the value of the difference, showing that the uncoupled decomposition is in reasonable agreement with the result of the coupled system. The individual contributions, the checksum value (uncoupled), and direct model output (coupled) are plotted as percentage changes from the reference case (function of TR) in Fig. 17.

In summary we see that overall cooling effectiveness (on mainstream-facing side of external wall; face 1) decreases with decreasing temperature ratio. The change is dominated by the change in film effectiveness and the ratio of mainstream-to-coolant heat transfer coefficients. The effect of Biot number is considered to be of intermediate importance and the effect of coolant warming factor is shown to be of only secondary importance.

Corresponding overall cooling effectiveness distributions on face 4 (plenum-facing side of internal wall) are shown in Fig. 18(a). On this wall the overall cooling effectiveness is dominated by the local temperature of the internal cooling flow (expressed non-dimensionally as the cooling warming factor,  $\chi$ ). This is due to extremely low heat transfer coefficient ( $h_4$ ) and driving temperature equal to coolant inlet temperature on the plenum-facing side of the internal wall. Nonetheless, the result is relevant because  $\theta_4$  is directly measured in the experiment. Percentage differences in internal wall overall cooling effectiveness from the reference case are shown in Fig. 18(b). Surface-averaged percentage changes across the plate surface are  $-0.15\%$ ,  $-0.30\%$ ,  $-0.46\%$ ,  $-0.66\%$ , and  $-0.90\%$  for  $T_{0m}/T_{0c} = 1.83, 1.67, 1.50, 1.33, 1.17$  respectively. As with face 1, the changes in overall cooling effectiveness with TR are monotonic, approximately linear in TR, but lower in magnitude by a factor of approximately  $1/4$ . The factor  $1/4$  is related to the coolant mass flow, and by extension the coolant flow specific heat

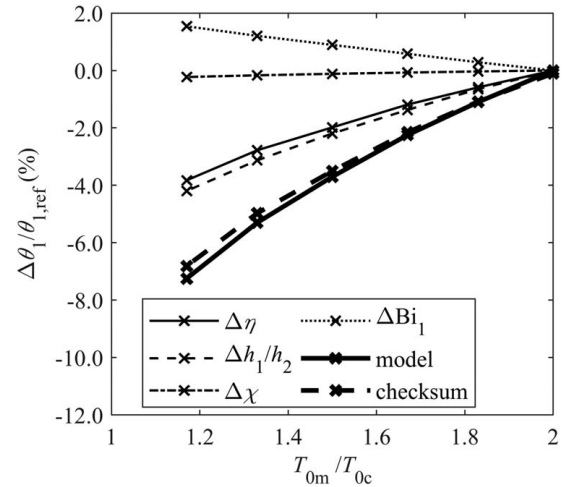


**Fig. 17 Percentage changes in overall cooling effectiveness showing: individual contributions from four dimensionless groups; the direct output of the model; and checksum (simple addition) of the four individual contributions**

capacity flux, and therefore the coolant heat pick up. The particular number is therefore particular to the coolant flow and not of fundamental significance. It is possible to recast Eq. (4) in a form relevant to face 4 by eliminating film effectiveness term ( $\eta$ ) as

$$\theta_4 = \frac{1 - \chi}{1 + Bi_4 + h_4/h_3} + \chi \quad (5)$$

As expected, performing a sensitivity analysis in similar manner to that shown for face 1 yields changes associated with the three groups which show the problem is entirely dominated by changes in coolant warming factor,  $\chi$ .

### Uncertainty Analysis

A detailed uncertainty analysis is presented in Appendix B, where we consider both the absolute uncertainty in  $\theta$  as a function of  $\theta$  and TR,  $U_\theta$ , and the uncertainty in  $\Delta \theta$  as a function of  $\Delta \theta$  and TR,  $U_{\Delta \theta}$ . The uncertainty analysis is based on Monte Carlo perturbation of Eq. (1), for normally distributed precision and bias uncertainties in the underlying temperatures. This is discussed in detail in Appendix B. In Table 8 we present summary results for face 1, showing: overall cooling effectiveness,  $\theta_1$ ; percentage uncertainty in  $\theta_1$ ,  $U_{\theta_1}/|\theta_1|$ ; absolute difference from reference condition,  $|\Delta \theta_1|$ ; and percentage uncertainty in difference from reference condition,  $U_{\Delta \theta_1}/|\Delta \theta_1|$ .

So far as the absolute uncertainty is concerned, we see that it is a strong function of TR: for TR = 1.17 the absolute uncertainty in  $\theta_1$

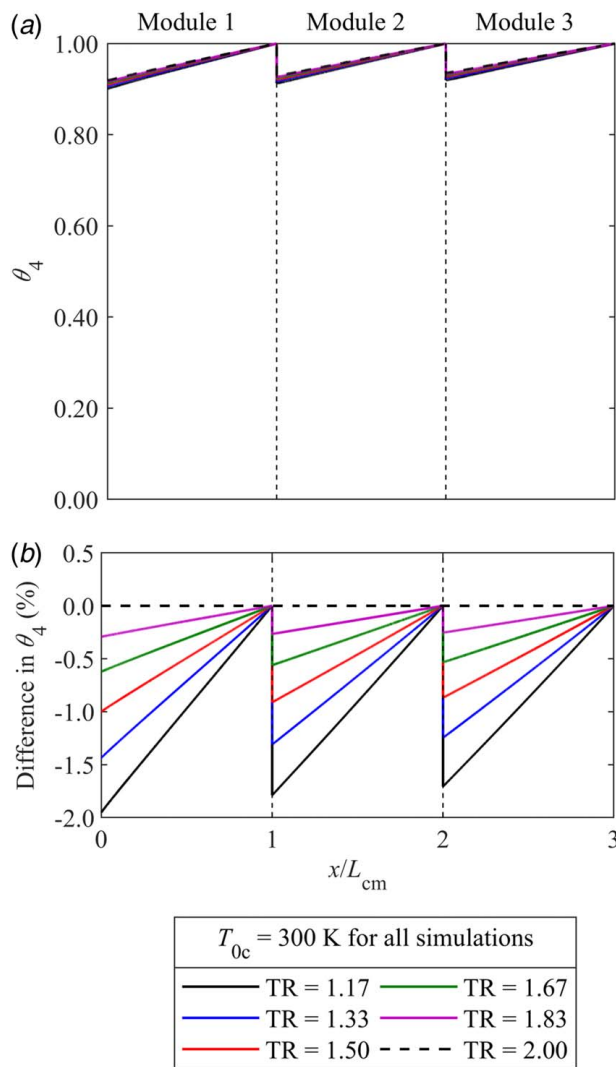


**Fig. 18 Results at six temperature ratios for fixed  $T_{0c}=300$  K for face 4: (a) overall cooling effectiveness distributions and (b) difference in overall cooling effectiveness from condition for  $T_{0m}/T_{0c}=2.00$**

**Table 8 Summary uncertainty analysis for face 1 showing: overall cooling effectiveness,  $\theta_1$ ; percentage uncertainty in  $\theta_1$ ,  $U_{\theta_1}/|\theta_1|$ ; absolute difference from reference condition,  $|\Delta\theta_1|$ ; and percentage uncertainty in difference from reference condition,  $U_{\Delta\theta_1}/|\Delta\theta_1|$**

$T_{0m}/T_{0c}$ (–)	$\theta_1$ (–)	$U_{\theta_1}/ \theta_1 $ (%)	$ \Delta\theta_1 $ (–)	$U_{\Delta\theta_1}/ \Delta\theta_1 $ (%)
2.00	0.454	0.732	–	–
1.83	0.449	0.894	0.0049	15.1
1.67	0.444	1.12	0.0102	8.58
1.50	0.437	1.54	0.0168	6.64
1.33	0.430	2.36	0.0241	6.68
1.17	0.421	4.66	0.0349	8.04

is 4.66% (for nominal value  $\theta_1=0.42$ ), falling to approximately 0.732% for  $TR=2.00$ . The absolute uncertainty decreases with temperature ratio because errors in individual temperatures are a smaller fraction of the temperature differences in the definition of  $\theta_1$  (Eq. (1)). The absolute errors are relatively small, even at modest temperature ratio, and fall to extremely low values for

high values or  $TR$ . That is, absolute values of  $\theta_1$  can be accurately determined in the experiment.

For our current purpose, it is the error in  $|\Delta\theta_1|$ , expressed as  $U_{\Delta\theta_1}/|\Delta\theta_1|$ , that is more important. This is because the primary purpose of the facility is comparison of overall cooling effectiveness at different temperature ratios. Here we define difference from the reference temperature ratio  $TR=2.00$ . At low separation from the reference temperature,  $TR=1.83$ , the percentage uncertainty in the difference  $\Delta\theta_1$  is 15.1%. As the separation increase, the percentage uncertainty drops to 6.64% (for  $TR=1.50$ ) before increasing slightly to 8.04% for  $TR=1.17$ . The relatively complex behavior is driven a combination of precision and bias errors in underlying measurements, and arises from considering of the degree of correlation of these errors between two particular temperature ratio conditions. This is discussed in detail in Appendix B. Most importantly, over most of our data range, the uncertainty in the difference  $\Delta\theta_1$  is more than an order of magnitude smaller than the difference itself. That is, the separation between temperature ratio conditions (prime purpose of facility) is easily resolved in this study.

## Conclusions

In this paper, we describe the low-order-model-based analysis of a facility designed to study scaling effects in systems with combined film and internal cooling. The new facility operates with engine-matched Mach number, Reynolds number, and coolant-to-mainstream pressure ratios, and allows tests of overall cooling effectiveness and adiabatic film effectiveness over a temperature ratio range from  $0.50 < T_{0m}/T_{0c} < 2.30$ . Results of commissioning tests on a fully-cooled (internal and film) metal plate demonstrate that high-quality spatially-resolved overall cooling effectiveness measurements can be obtained.

CFD simulations were carried out to determine the adiabatic film effectiveness distributions for fixed  $Re_D$ ,  $M$ , and  $p_{0c}/p_{0m}$ , but over a temperature ratio range  $0.50 < T_{0m}/T_{0c} < 2.30$ . Surface-averaged changes in adiabatic film effectiveness (from case with  $T_{0m}/T_{0c}=2.00$ ) were  $-6.55\%$ ,  $-8.20\%$ ,  $-12.44\%$ ,  $-15.61\%$ , and  $-17.43\%$  for  $T_{0m}/T_{0c}=1.83$ ,  $1.67$ ,  $1.50$ ,  $1.33$ , and  $1.17$  respectively. The decrease in adiabatic film effectiveness with temperature ratio was monotonic, approximately linear, and driven primarily by a decrease in the coolant-to-mainstream specific heat capacity flux ratio. Lower relative heat storage capacity of the film cooling flow compared to the entrained mainstream flow leads to a greater relative temperature increase of the missing layer.

A low-order conjugate thermal model was used to predict the expected separation between overall cooling effectiveness distributions over the range of facility temperature ratios for fixed  $Re_D$ ,  $M$ , and  $p_{0c}/p_{0m}$ . Overall cooling effectiveness was found to decrease with decreasing temperature ratio, with predicted percentage changes from the reference condition ( $T_{0m}/T_{0c}=2.00$ ) in external wall overall cooling effectiveness of  $-1.10\%$ ,  $-2.25\%$ ,  $-3.70\%$ ,  $-5.30\%$ , and  $-7.25\%$  for  $T_{0m}/T_{0c}=1.83$ ,  $1.67$ ,  $1.50$ ,  $1.33$ , and  $1.17$  respectively. The decrease was monotonic, approximately linear, and found to be driven largely by the decrease in external film effectiveness (+55% of change) and the increase in the ratio of mainstream-to-coolant heat transfer coefficients (+60% of change). Secondary influences were a Biot number effect (–20% of change) and a change in the internal coolant warming factor coolant factor (+4.50% of change).

To emphasize a key point, a typical nozzle guide vane which at engine conditions ( $TR=2.00$ ) would have overall cooling effectiveness of 0.450 would be expected to have overall effectiveness of 0.418 at typical rig conditions with  $TR=1.20$  (correct, interpolated numbers). That is, typical scaling from engine-to-rig result is  $-7.1\%$ , and typical scaling from rig-to-engine is  $+7.7\%$ . This result is important for first order estimation of overall cooling performance at engine conditions. We recall that this is in the practical situation of co-dependent variation of all non-dimensional groups



as temperature ratio is varied, and not a study of the effect of variation of temperature ratio in isolation, i.e., the situation of most relevance and importance to engine designers.

On the internal wall facing the coolant plenum, changes in overall effectiveness were smaller (approximately 1/4 that of external wall) and entirely dominated by the coolant warming factor. The factor 1/4 was related to the coolant mass flow, and by extension the coolant flow specific heat capacity flux, and therefore the coolant heat pick up. The particular number is therefore particular to the coolant flow and not of fundamental significance.

A detailed uncertainty analysis is presented which shows that the uncertainty in the difference  $\Delta\theta_1$  is more than an order of magnitude smaller than the difference itself. That is, the separation between temperature ratio conditions (prime purpose of facility) is easily resolved by measurements in the facility.

The issue of scaling overall effectiveness measurements between typical rig (TR = 1.20) and engine (TR = 2.00) conditions is not yet fully resolved, but is of central importance in the drive for high-accuracy high-TRL (technology readiness level) validation studies of overall cooling system performance. These play a role both in component optimization (research) and engine design validation (thermal paint test engine or equivalent). It is hoped that this bespoke facility, and associated analysis, simulation, and processing methods will play a key role in validating rig-to-engine scaling methods.

## Acknowledgment

The financial support of Rolls-Royce Plc and Innovate UK are gratefully acknowledged.

## Conflict of Interest

There are no conflicts of interest.

## Data Availability Statement

The authors attest that all data for this study are included in the paper.

## Nomenclature

$h$	= heat transfer coefficient ( $\text{W m}^{-2} \text{K}^{-1}$ )
$k$	= thermal conductivity ( $\text{W m}^{-1} \text{K}^{-1}$ )
$l$	= turbulence length scale (m)
$p$	= pressure (Pa)
$t$	= time (s)
$x$	= axial position (m)
$y$	= lateral position (m)
$D$	= hole diameter (m)
$I$	= momentum flux ratio (–)
$L$	= length (m)
$M$	= Mach number (–)
$T$	= temperature (K)
$U$	= uncertainty (–)
$\dot{m}$	= mass flowrate ( $\text{kg s}^{-1}$ )
$c_p$	= specific heat capacity ( $\text{J kg}^{-1} \text{K}^{-1}$ )
$y^+$	= non-dimensional wall distance (–)
$Nu$	= Nusselt number (–)
$Pr$	= Prandtl number (–)
$Tu$	= turbulence intensity (%)
$Bi$	= Biot number (–)
$BR$	= blowing ratio (–)
$DR$	= density ratio (–)
$ER$	= specific heat capacity flux ratio (–)
$TR$	= temperature ratio (–)
$VR$	= velocity ratio (–)
$Re_D$	= Reynolds number based on cooling hole diameter and mainstream velocity (–)

## Greek Symbols

$\gamma$	= ratio of specific heat capacities (–)
$\eta$	= adiabatic film effectiveness (–)
$\theta$	= overall cooling effectiveness (–)
$\mu$	= dynamic viscosity ( $\text{Pa s}$ )
$\rho$	= density ( $\text{kg m}^{-3}$ )
$\tau$	= wall shear stress (Pa)
$\tau$	= thermal time constant (s)
$\chi$	= coolant warming factor (–)

## Subscripts

0	= total condition
1	= external wall facing mainstream
2	= external wall facing coolant channel
3	= internal wall facing coolant channel
4	= internal wall facing coolant plenum
c	= coolant
e	= entrainment
f	= film
m	= mainstream
w	= wall
aw	= adiabatic wall
cm	= cooled modules
in	= inlet
ext	= external
int	= internal
out	= outlet
CFD	= computational fluid dynamics
CL	= centerline
LA	= laterally-averaged
SA	= surface-averaged

## Abbreviations

CFD	= computational fluid dynamics
IR	= infrared
LE	= leading edge
TE	= trailing edge

## Appendix A: Estimation of Thermal Time Constant for Metal and Ceramic Flat-Plates

To estimate the thermal time constants for the metal and ceramic flat-plates, a 1D transient thermal model was used. External and internal wall thermal resistances were modeled, with surfaces coupled to the adjacent fluid described by representative (typical) temperature and heat transfer coefficient boundary condition. The 1D model is shown schematically in Fig. 19. Explicit finite differencing was used with approximately 25 through-wall cells and a time-step size of  $1.50 \times 10^{-3}$  s (chosen for solution stability). Fixed boundary conditions were  $T_{0m} = 600$  K,  $T_{0c,in} = 300$  K,  $h_1 = 520$   $\text{W m}^{-2} \text{K}^{-1}$ ,  $h_2 = 310$   $\text{W m}^{-2} \text{K}^{-1}$ ,  $h_3 = 105$   $\text{W m}^{-2} \text{K}^{-1}$ , and

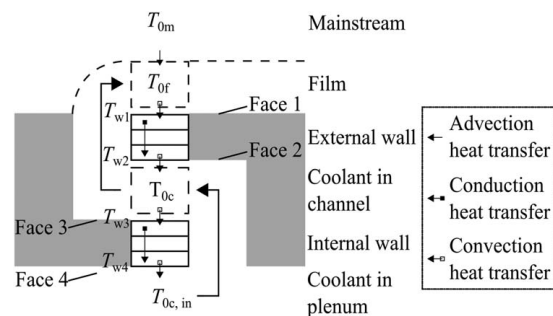
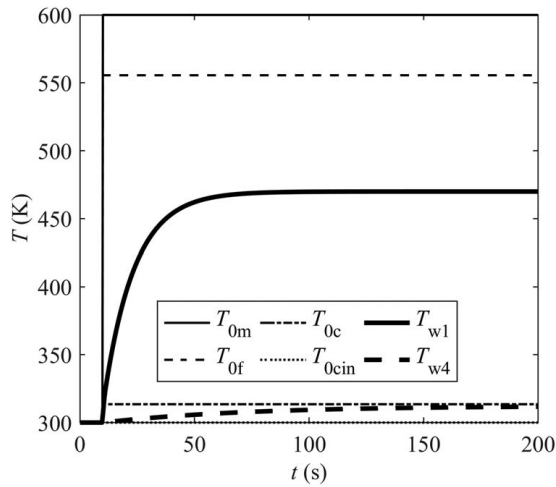


Fig. 19 Schematic representation of the 1D transient thermal model



**Fig. 20** Predicted transient temperature characteristics for the mainstream flow, coolant flow, and for face 1 and face 4 for the metal test plate

$h_4 = 10 \text{ W m}^{-2} \text{ K}^{-1}$  (average of  $h$  in Fig. 15(a)). The film temperature was taken to be  $T_{0f} = 555 \text{ K}$  (from average of  $\eta$  in Fig. 15(c)). The average coolant temperature in the channel was taken to be  $T_{0c} = 315 \text{ K}$  (from average of  $\epsilon$  in Fig. 15(c)). Mainstream, film, and coolant-channel temperatures are defined to have a step change to their respective values from 300 K at  $t = 10 \text{ s}$ .

The resulting transient wall temperatures on face 1 (mainstream-facing side of external wall) and face 4 (plenum-facing side of internal wall) are shown in Fig. 20. Taking a best-fit in the form of the lumped-heat-capacitor response equation for face 1

$$\frac{T_{w1}(t) - T_{0m}(t=0)}{T_{0m}(t=\infty) - T_{0m}(t=0)} = 1 - e^{-t/\tau} \quad (\text{A1})$$

we evaluate a time constant for face 1 equal to  $\tau_1 = 12.2 \text{ s}$ . Performing a similar method for face 4 gives  $\tau_4 = 62.8 \text{ s}$ . These values are small compared to the thermal time constant of the facility (approximately 500 s, see Fig. 9). Quasi-steady conditions of overall cooling effectiveness (defined to be within 1% of the time-local steady-state value) are reached after 170 s for typical inlet temperature characteristics (see Fig. 9) for the facility.

## Appendix B: Uncertainty Analysis

In this section we consider the absolute uncertainty in  $\theta$  as a function of  $\theta$  and TR,  $U_\theta$ , and the uncertainty in  $\Delta\theta$  as a function of  $\Delta\theta$  and TR,  $U_{\Delta\theta}$ . The uncertainty analysis is based on Monte Carlo perturbation of Eq. (1), for normally distributed precision and bias uncertainties in the underlying temperatures.

In our analysis it is assumed that uncertainties in mainstream, coolant, and wall temperatures are dominated by uncertainties in thermocouple measurements (or thermocouple-based calibration methods; see Michaud et al. [41]) of each of the three temperatures. The assumption is discussed in detail in Michaud et al. [45]. Although there are properly other errors associated with the IR processing method that is used to determine wall temperature, including window transmissivity error and surface emissivity error (see detailed analysis in Kirillos and Povey [28]), these are small in comparison to the thermocouple calibration error, and our analysis we neglect them. This is partially justified by the magnitude of the errors, but, so far as the errors in transmissivity and emissivity are concerned, these can—quite accurately—be taken to be constant and independent of TR, and therefore fully correlated between temperature ratios. That is, so far as the error in  $\Delta\theta$  is concerned (as opposed to the error in  $\theta$ ), these terms drop out of the analysis.

We take the quoted bias uncertainty for K-type thermocouple measurements as  $\pm 1.10 \text{ K}$  (higher accuracy thermocouples, with

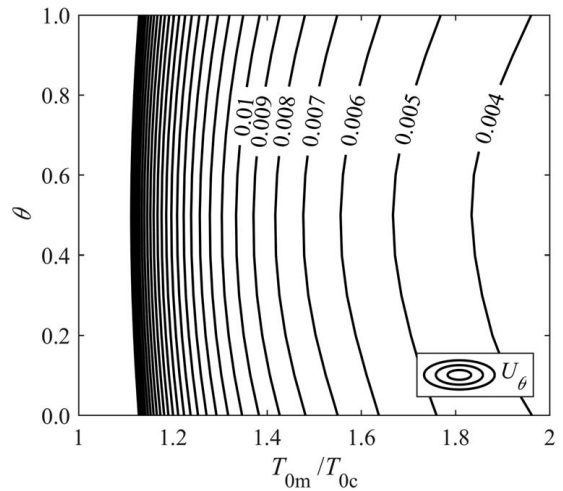


**Fig. 21** Contours of uncertainty in  $\theta$ ,  $U_\theta$ , as a function of  $\theta$  and TR

so-called *special limits of error*). We do *not* perform  $1/\sqrt{N}$  reduction (where  $N$  is the number of thermocouples); i.e., we do not assume the individual thermocouples are uncorrelated in their response characteristics. This assumption allows worst-case error estimation. The bias uncertainty is caused by cold junction compensation drift, differences individual thermocouple characteristics, and non-linearity and hysteresis characteristics. We take the first term to be small, and deal with the second two terms by applying an offset modeled as third-order polynomial in  $T$ , arranged to have three inflection points randomly distributed (per run; per thermocouple) in the ranges  $300 \text{ K} < T < 600 \text{ K}$  with normally distributed magnitudes with three-sigma bands  $\pm 1.10 \text{ K}$ . We assume that coolant temperatures are uncontrolled in the range  $290 \text{ K} < T_{0c} < 300 \text{ K}$  (day-to-day variation). A Monte Carlo simulation was performed in the range  $0.0 < \theta < 1.0$  and  $1.0 < \text{TR} < 2.0$  with 100 steps in each axis, with 100 simulations per point, i.e.,  $1.0 \times 10^6$  simulations in total. Sampling rate was sufficient (500 Hz) that precision uncertainty due to sample size becomes negligible; we ignore this component. The outputs of the Monte Carlo simulation are—approximately normal—distributions of temperatures  $T_{w1}$ ,  $T_{w4}$ ,  $T_{0m}$ , and  $T_{0c}$  (on grid of  $\theta$  and TR). From this uncertainty limits on  $\theta$  and  $\Delta\theta$  ( $U_\theta$  and  $U_{\Delta\theta}$ , respectively) can be calculated.

Consider first the uncertainty distribution  $U_\theta$  (function of TR and  $\theta$ ) in Fig. 21.  $U_\theta$  decreases with increasing TR. This is because

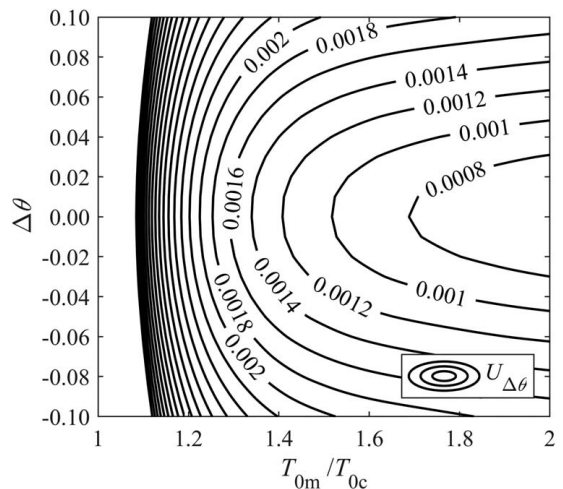


**Fig. 22** Contours of uncertainty in  $\Delta\theta$ ,  $U_{\Delta\theta}$ , as a function of  $\Delta\theta$  and TR for  $\theta = 0.45$

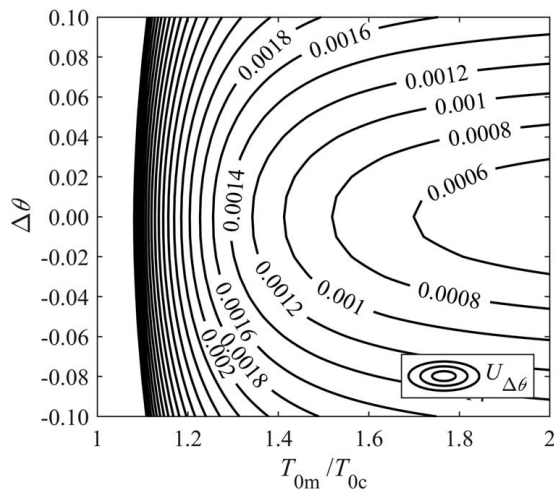


**Fig. 23** Contours of uncertainty in  $\Delta\theta$ ,  $U_{\Delta\theta}$ , as a function of  $\Delta\theta$  and TR for  $\theta = 0.95$

absolute uncertainties in underlying values are a smaller proportion of the temperature differences in the numerator and denominator of Eq. (1) as the TR increases. There is only modest dependence of the result on  $\theta$ . For the reference condition TR = 2.0, the uncertainty is estimated to be  $U_\theta = 0.00333$ . For a reference value  $\theta = 0.50$  this is equivalent to an error of 0.66%.

Now consider the uncertainty distribution  $U_{\Delta\theta}$  (function of TR and  $\Delta\theta$ ), which is presented in Figs. 22 and 23 for values  $\theta = 0.45$  (typical of face 1) and  $\theta = 0.95$  (typical of face 4) respectively. The distributions of  $U_{\Delta\theta}$  are similar for the two values  $\theta$ :  $U_{\Delta\theta}$  decreases with increasing TR due to the corresponding decrease in  $U_\theta$ ; at higher TR,  $U_{\Delta\theta}$  also decreases with decreasing  $\Delta\theta$  due to increasing correlation between the two temperature measurements used to determine the two values of  $\theta$ . Comparing Fig. 22 ( $\theta = 0.45$ ) and Fig. 23 ( $\theta = 0.95$ ) we see there is only modest dependence on the absolute value of  $\theta$ , with slightly lower values of  $U_{\Delta\theta}$  as  $\theta$  increases.

## References

- [1] Baldauf, S., Schulz, A., and Wittig, S., 2001, "High-Resolution Measurements of Local Effectiveness From Discrete Hole Film Cooling," *ASME J. Turbomach.*, **123**(4), pp. 758–765.
- [2] Baldauf, S., Schulz, A., and Wittig, S., 2001, "High-Resolution Measurements of Local Heat Transfer Coefficients From Discrete Hole Film Cooling," *ASME J. Turbomach.*, **123**(4), pp. 749–757.
- [3] Straub, D. L., Sidwell, T. G., Casleton, K. H., Alvin, M. A., Chien, S., and Chyu, M. K., 2012, "High Temperature Film Cooling Test Facility and Preliminary Test Results," Proceedings of ASME Turbo Expo 2012, Copenhagen, Denmark, June 11–15, Paper No. GT2012-69767.
- [4] Wiers, S. H., Fransson, T. H., Radeklint, U., and Annerfeldt, M., "Flow Field Measurements in a Cold Flow Annular Sector Turbine Cascade Test Facility and an Annular Sector Cascade Test Facility Operating at Near-Engine Conditions," Proceedings of ASME Turbo Expo 2001, New Orleans, LA, June 4–7, Paper No. 2001-GT-0491.
- [5] Paniagua, G., Cuadrado, D., Saavedra, J., Andreoli, V., Meyer, T., Solano, J. P., Herrero, R., Meyer, S., and Lawrence, D., 2019, "Design of the Purdue Experimental Turbine Aerothermal Laboratory for Optical and Surface Aerothermal Measurements," *ASME J. Eng. Gas Turbines Power*, **141**(1), p. 012601.
- [6] Messenger, A., and Povey, T., 2020, "Calibrated Low-Order Transient Thermal and Flow Models for Robust Test Facility Design," *J. Glob. Power Propul. Soc.*, **4**, pp. 94–113.
- [7] Kirollos, B., Lubbock, R., Beard, P., Goenaga, F., Rawlinson, A., Janke, E., and Povey, T., 2017, "ECAT: An Engine Component Aerothermal Facility at the University of Oxford," Proceedings of ASME Turbo Expo 2017, Charlotte, NC, June 26–30, Paper No. GT2017-64736.
- [8] Michaud, M., Ormano, F., and Povey, T., 2023, "Annular Dump Diffuser and Deswirl System for Back-Pressure Control in Engine-Scale Transonic Annular Cascade," *ASME J. Turbomach.*, **145**(4), p. 041006.
- [9] Jones, T. V., 1999, "Theory for the Use of Foreign Gas in Simulating Film Cooling," *J. Heat Fluid Flow*, **20**(3), pp. 349–354.
- [10] Pedersen, D. R., Eckert, E. R. G., and Goldstein, R. J., 1977, "Film Cooling With Large Density Differences Between the Mainstream and the Secondary Fluid

Measured by the Heat-Mass Transfer Analogy," *ASME J. Heat Transfer-Trans. ASME*, **99**(4), pp. 620–627.

- [11] Teekaram, A. J. H., Forth, C. J. P., and Jones, T. V., 1989, "The Use of Foreign Gas to Simulate the Effects of Density Ratios in Film Cooling," *ASME J. Turbomach.*, **111**(1), pp. 57–62.
- [12] Liu, K., Yang, S. F., and Han, J. C., 2012, "Influence of Coolant Density on Turbine Blade Film-Cooling With Compound-Angle Shaped Holes," Proceedings of ASME Turbo Expo 2012, Copenhagen, Denmark, June 11–15, Paper No. GT2012-69117.
- [13] Narzary, D. P., Liu, K. C., Rallabandi, A. P., and Han, J. C., 2012, "Influence of Coolant Density on Turbine Blade Film-Cooling Using Pressure Sensitive Paint Technique," *ASME J. Turbomach.*, **134**(3), p. 031006.
- [14] Ormano, F., and Povey, T., 2020, "Theory of Non-Dimensional Groups in Film Effectiveness Studies," *ASME J. Turbomach.*, **142**(4), p. 041002.
- [15] Thole, K. A., Sinha, A. K., and Bogard, D. G., 1990, "Mean Temperature Measurements of Jets With a Crossflow for Gas Turbine Film Cooling," Proceedings of the Third International Symposium on Transport Phenomena and Dynamics of Rotating Machinery (ISROMAC-3), Honolulu, HI, April 1–4.
- [16] Sinha, A. K., Bogard, D. G., and Crawford, M. E., 1991, "Film Cooling Effectiveness Downstream of a Single Row of Holes With Variable Density Ratio," *ASME J. Turbomach.*, **113**(4), pp. 442–449.
- [17] Ethridge, M. I., Cutbirth, J. M., and Bogard, D. G., 2001, "Scaling of Performance for Varying Density Ratio Coolants on an Airfoil With Strong Curvature and Pressure Gradient Effects," *ASME J. Turbomach.*, **123**(2), pp. 231–237.
- [18] Baldauf, S., Scheulen, M., Schulz, A., and Wittig, S., 2002, "Correlation of Film-Cooling Effectiveness From Thermographic Measurements at Enginelike Conditions," *ASME J. Turbomach.*, **124**(4), pp. 686–698.
- [19] Baldauf, S., Scheulen, M., Schulz, A., and Wittig, S., 2002, "Heat Flux Reduction From Film Cooling and Correlation of Heat Transfer Coefficients From Thermographic Measurements at Enginelike Conditions," *ASME J. Turbomach.*, **124**(5), pp. 699–709.
- [20] Dees, J. E., Bogard, D. G., Ledezma, G. A., Laskowski, G. M., and Tolpadi, A. K., 2012, "Experimental Measurements and Computational Predictions for an Internally Cooled Simulated Gas Turbine Vane With 90 Degree Rib Turbulators," *ASME J. Turbomach.*, **134**(6), p. 061005.
- [21] Dees, J. E., Bogard, D. G., Ledezma, G. A., Laskowski, G. M., and Tolpadi, A. K., 2012, "Experimental Measurements and Computational Predictions for an Internally Cooled Simulated Turbine Vane," *ASME J. Turbomach.*, **134**(6), p. 061003.
- [22] Dees, J. E., Bogard, D. G., Ledezma, G. A., and Laskowski, G. M., 2013, "Overall and Adiabatic Effectiveness Values on a Scaled-Up, Simulated Gas Turbine Vane," *ASME J. Turbomach.*, **135**(5), p. 051017.
- [23] Dyson, T. E., McClintic, J. W., Bogard, D. G., and Bradshaw, S. D., 2013, "Adiabatic and Overall Effectiveness for a Fully Cooled Turbine Vane," Proceedings of ASME Turbo Expo 2013, San Antonio, TX, June 3–7, Paper No. GT2013-94928.
- [24] Nathan, M. L., Dyson, T. E., Bogard, D. G., and Bradshaw, S. D., 2014, "Adiabatic and Overall Effectiveness for the Showerhead Film Cooling of a Turbine Vane," *ASME J. Turbomach.*, **136**(3), p. 031005.
- [25] Luque, S., Aubry, J., and Povey, T., 2009, "A New Engine-Parts Annular Sector Cascade to Prove NGV Cooling Systems," Proceedings of the Eighth European Conference on Turbomachinery, Graz, Austria, Mar. 23–27.
- [26] Luque, S., and Povey, T., 2011, "A Novel Technique for Assessing Turbine Cooling System Performance," *ASME J. Turbomach.*, **133**(3), p. 031013.
- [27] Luque, S., Batstone, J., Gillespie, D. R. H., Povey, T., and Romero, E., 2014, "Full Thermal Experimental Assessment of a Dendritic Turbine Vane Cooling Scheme," *ASME J. Turbomach.*, **136**(2), p. 021011.
- [28] Kirollos, B., and Povey, T., 2017, "Laboratory Infrared Thermal Assessment of Laser-Sintered High-Pressure Nozzle Guide Vanes to Derisk Engine Design Programs," *ASME J. Turbomach.*, **139**(4), p. 041009.
- [29] Forth, C. J. P., Loftus, P. J., and Jones, T. V., 1985, "The Effect of Density Ratio on the Film-Cooling of a Flat Plate," Symposium on Heat Transfer and Cooling in Gas Turbines, Paper No. AGARD-CP-390.
- [30] Forth, C. J. P., and Jones, T. V., 1986, "Scaling Parameters in Film-Cooling," Proceedings of the Eighth International Heat Transfer Conference, San Francisco, CA, Aug. 17–22.
- [31] Rutledge, J. L., and Polanka, M. D., 2014, "Computational Fluid Dynamics Evaluations of Unconventional Film Cooling Scaling Parameters on a Simulated Turbine Blade Leading Edge," *ASME J. Turbomach.*, **136**(10), p. 101006.
- [32] Luque, S., Jones, T. V., and Povey, T., 2016, "Theory for the Scaling of Metal Temperatures in Cooled Compressible Flows," *Int. J. Heat Mass Transfer*, **102**, pp. 331–340.
- [33] Luque, S., Jones, T. V., and Povey, T., 2017, "Effects of Coolant Density, Specific Heat Capacity, and Biot Number on Turbine Vane Cooling Effectiveness," *ASME J. Turbomach.*, **139**(11), p. 111005.
- [34] Williams, R. P., Dyson, T. E., Bogard, D. G., and Bradshaw, S. D., 2014, "Sensitivity of the Overall Effectiveness to Film Cooling and Internal Cooling on a Turbine Vane Suction Side," *ASME J. Turbomach.*, **136**(3), p. 031006.
- [35] BSI, 2003, "Measurement of Fluid Flow by Means of Pressure Differential Devices Inserted in Circular Cross-Section Conduits Running Full," Technical Report, British Standards Institution, London, UK, Report No. BS EN ISO 5167.
- [36] Morel, T., 1975, "Comprehensive Design of Axisymmetric Wind Tunnel Contractions," *ASME J. Fluids Eng.*, **97**(2), pp. 225–233.



- [37] Morel, T., 1977, "Design of Two-Dimensional Wind Tunnel Contractions," *ASME J. Fluids Eng.*, **99**(2), pp. 371–377.
- [38] Su, Y., 1991, "Flow Analysis and Design of Three-Dimensional Wind Tunnel Contractions," *AIAA J.*, **29**(11), pp. 1912–1920.
- [39] Roach, P. E., 1987, "The Generation of Nearly Isotropic Turbulence by Means of Grids," *Int. J. Heat Fluid Flow*, **8**(2), pp. 82–92.
- [40] Ishikawa, K., and Nakamura, I., 1990, "Performance Chart and Optimum Geometries of Conical Diffusers With Uniform Inlet Flow and Tailpipe Discharge," *JSME Int. J.*, **33**(1), pp. 97–105.
- [41] Michaud, M., Ornano, F., Chowdhury, N. H. K., and Povey, T., 2020, "Methodology for High-Accuracy Infrared Calibration in Environments With Through-Wall Heat Flux," *J. Glob. Power Propul. Soc.*, **4**, pp. 1–13.
- [42] Kirolos, B., and Povey, T., "Reverse-Pass Cooling Systems for Improved Performance," Proceedings of ASME Turbo Expo 2014, Duesseldorf, Germany, June 16–20, Paper No. GT2014-25901.
- [43] Kirolos, B., and Povey, T., 2016, "Cooling Optimization Theory—Part I: Optimum Wall Temperature, Coolant Exit Temperature, and the Effect of Wall/Film Properties on Performance," *ASME J. Turbomach.*, **138**(8), p. 081002.
- [44] Kirolos, B., and Povey, T., 2016, "Cooling Optimization Theory—Part II: Optimum Internal Heat Transfer Coefficient Distribution," *ASME J. Turbomach.*, **138**(8), p. 081003.
- [45] Michaud, M., Chowdhury, N. H. K., and Povey, T., 2023, "Experimental Study of Impact of In-Service Deterioration on Thermal Performance of High Pressure Nozzle Guide Vanes," *ASME J. Turbomach.*, **145**(2), p. 021014.
- [46] Poferl, D. J., and Svehla, R. A., 1973, "Thermodynamic and Transport Properties of Air and Its Products of Combustion With ASTM-A-1 Fuel and Natural Gas at 20, 30 and 40 Atmospheres," Technical Note, NASA, Cleveland, OH, Report No. NASA TN D-7488.
- [47] Poferl, D. J., Svehla, R. A., and Lewandowski, K., 1969, "Thermodynamic and Transport Properties of Air and the Combustion Products of Natural Gas and of ASTM-A-1 Fuel With Air," Technical Note, NASA, Cleveland, OH, Report No. NASA TN D-5452.
- [48] Kirolos, B., and Povey, T., 2015, "An Energy-Based Method for Predicting the Additive Effect of Multiple Film Cooling Rows," *ASME J. Eng. Gas Turbines Power*, **137**(12), p. 122607.
- [49] Kirolos, B., and Povey, T., 2017, "Method for Accurately Evaluating Flow Capacity of Individual Film-Cooling Rows of Engine Components," *ASME J. Turbomach.*, **139**(11), p. 111004.
- [50] Zielinska, M., Yavorska, M., Poreba, M., and Sieniawski, J., 2010, "Thermal Properties of Cast Nickel Based Superalloys," *Arch. Mater. Sci. Eng.*, **44**(1), pp. 35–38.
- [51] Thomas, M., and Povey, T., 2016, "A Novel Scalar Tracking Method for Optimising Film Cooling Systems," *Proc. Inst. Mech. Eng. A: J. Power Energy*, **230**(1), pp. 3–15.